

## The effect of Langmuir turbulence under complex real oceanic and meteorological forcing

Yalin Fan <sup>a,\*</sup>, Zhitao Yu <sup>a</sup>, Ivan Savelyev <sup>b</sup>, Peter P. Sullivan <sup>c</sup>, Jun-Hong Liang <sup>d</sup>, Tracy Haack <sup>e</sup>, Eric Terrill <sup>f</sup>, Tony de Paolo <sup>f</sup>, Kipp Shearman <sup>g</sup>

<sup>a</sup> US Naval Research Laboratory, Stennis Space Center, MS, United States of America

<sup>b</sup> US Naval Research Laboratory, Washington, DC, United States of America

<sup>c</sup> National Center for Atmospheric Research, Boulder, CO, United States of America

<sup>d</sup> Louisiana State University, Baton Rouge, LA, United States of America

<sup>e</sup> US Naval Research Laboratory, Monterey, CA, United States of America

<sup>f</sup> Scripps Institution of Oceanography, La Jolla, CA, United States of America

<sup>g</sup> Oregon State University, Corvallis, OR, United States of America

### A B S T R A C T

In this study, we expand previous large eddy simulation (LES) modeling investigations of Langmuir turbulence (LT) to real ocean conditions using field observations collected under the multi-platform field campaign “Coupled Air–Sea Processes and Electromagnetic (EM) ducting Research (CASPER-East)”. The measurement site has strong local variabilities of temperature and salinity and experienced large variations in wind forcing and several cooling events.

Although LT enhances the turbulence in the water column and deepens the mixed layer during most of the simulation period, being consistent with previous studies, strong reduction of turbulent kinetic energy (TKE) in the mixed layer is observed in the simulation with Stokes drift compared to that without Stokes drift during a short period. Analysis of the meteorological forcing and the TKE budget have revealed that in the circumstance of swell dominated wave fields with young wind seas, the presence of Stokes drift reduces shear production more than the Stokes production it generates, and a reduction of total TKE in the mixed layer may be expected whether or not the Stokes drift is aligned with the wind.

Weak reduction of TKE due to the inclusion of Stokes drift is also observed beneath the mixed layer during a cooling event possibly due to the fact that the upwelling associated with Langmuir circulation at the base of the mixed layer counteracts on the downwelling associated with the deep convection and reduces the total turbulence level in the water column.

While both resolved Reynold stresses and the bulk eddy viscosity decrease with the increase of wind-wave misalignment angle  $\theta_{ww}$  and become smaller than that in the case without Stokes drift when  $\theta_{ww}$  exceed  $60^\circ$ , the subgrid scale (SGS) part of the momentum flux increases with the increase of  $\theta_{ww}$ , suggesting that the LES solutions in cases with large wind-wave misalignment become more sensitive to the SGS models used and need to be dealt with caution.

### 1. Introduction

Langmuir turbulence (LT) is believed to be one of the leading order causes of turbulent mixing in the upper ocean, which is important for momentum and heat exchange across the air–sea interface and between the mixed layer and the thermocline. Both observational studies (D’Asaro, 2001, 2014) and large-eddy simulation (LES) investigations (Li et al., 1995; Kukulka et al., 2009, 2010; Skylingstad and Denbo, 1995; McWilliams et al., 1997; Hamlington et al., 2014) have shown enhanced vertical mixing within the ocean surface boundary layer in the presence of LT through the enhanced vertical turbulent velocity variance.

The dynamical origin of Langmuir circulation is understood as wind-driven shear instability in combination with surface wave influences related to their mean Lagrangian motion, called Stokes drift. The prevailing theoretical interpretation of Langmuir circulation is derived by Craik and Leibovich (1976), where they introduced the effect of

waves on Eulerian mean flow into the Navier–Stokes equations. Even though the theory was developed four decades ago, scientists were not able to adequately measure or simulate LT until thirty years ago. While LES models have been used to simulate Langmuir circulation in the upper ocean, yielding new insights that could not be obtained from field observations or turbulent closure models, most of these studies were conducted under idealized conditions with simplified oceanic and wind conditions (Skylingstad and Denbo, 1995; McWilliams et al., 1997, 2012; Sullivan et al., 2012; Hamlington et al., 2014; Reichl et al., 2016). Idealizing and isolating individual processes makes it easier to study their effects, but can also unrealistically magnify or underestimate their impact, due to the lack of complex and non-linear interactions of multiple dynamical processes taking place in the real ocean. Thus, parameterizations that have developed from these idealized studies can have limited practical application in ocean modeling. For example, evaluation of three of the K profile parameterizations (KPP, developed by Large et al., 1994) with LT modifications

\* Correspondence to: Oceanography Division, Naval Research Laboratory, Stennis Space Center, MS 39529, United States of America.  
E-mail address: [yalin.fan@nrlssc.navy.mil](mailto:yalin.fan@nrlssc.navy.mil) (Y. Fan).

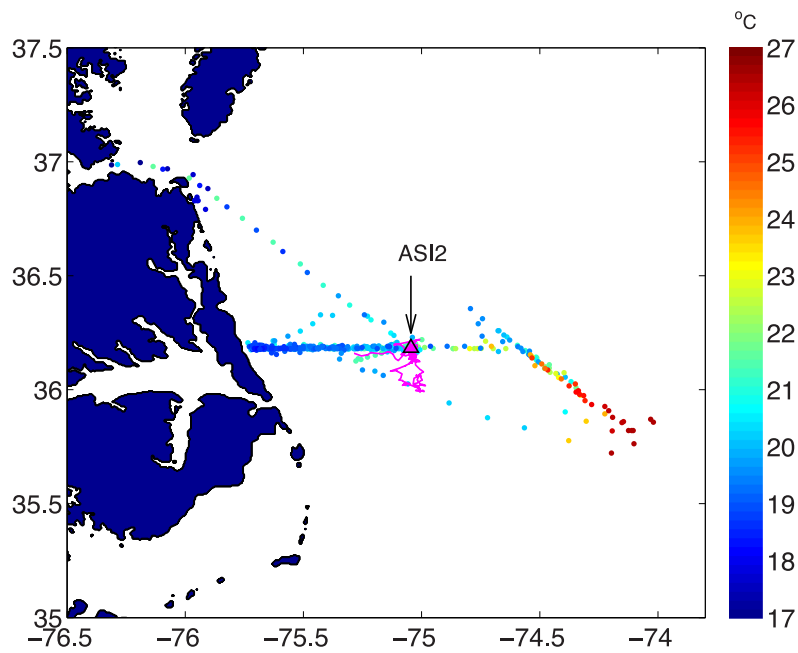


Fig. 1. Track of the research boat color-coded with its sea surface temperature measurements as indicated in the color bar. The magenta line gives the track of the glider, and the black triangle shows the location of supersite ASI2.

(McWilliams and Sullivan, 2000; Smyth et al., 2002; Qiao et al., 2004) in the GFDL climate model have shown that none of the schemes give consistent improvement to ocean circulation models globally most likely due to their lack of interaction with ocean physics (Fan and Griffies, 2014). While in Li et al. (2016) and Li and Fox-Kemper (2017), substantial improvements are observed when more physical processes are considered in the scaling, such as Harcourt and D'Asaro (2008) and Van Roekel et al. (2012).

In this study, we expand the previous LES modeling investigations of LT to real ocean conditions. Model forcing and initial conditions are obtained from a multi-platform field campaign, “Coupled Air–Sea Processes and Electromagnetic (EM) ducting Research (CASPER-East)” that took place off the coast of North Carolina in late October to early November of 2015. The study location, approximately 63 km east of Duck, N.C., is frequently influenced by fresher and cooler water inflow from nearby rivers and bays and warmer and saltier water intrusion from the Gulf stream, and experienced several cooling events and dramatic turning of wind directions due to storm passage during the observation period. Temperature (T) and salinity (S) profiles, surface gravity wave spectra, and meteorological forcing data were collected during the CASPER-East campaign, providing a rich data set to study the effect of LT on the dynamics and structure of the oceanic mixed layer under complex oceanic and meteorological conditions. The outline of this paper is as follows. A brief description of the observations during the CASPER-East experiment, the LES model used for this study, and the experiment set up are given in Section 2. Results are analyzed in Section 3, and discussion and concluding remarks are presented in Section 4.

## 2. Method

### 2.1. Observations

The field data used in this research was collected under the CASPER project aimed to improve the characterization of the propagation of radio frequency signals through the marine atmosphere (Wang et al., 2018a). CASPER-East, the first of two major field campaigns during the CASPER project, was conducted from October 10 to November 6

of 2015 off the coast of North Carolina, eastward from the US Army Corps of Engineers Field Research Facility pier at Duck.

Atmospheric and oceanic measurements used in this paper were collected around an air–sea interaction supersite (ASI2) established at (36.1837N, 75.0451W), approximately 63 kilometers east of the shoreline (Fig. 1). Due to the effect of near shore cooler and fresher water to the west and warmer and saltier water along the Gulf stream (GS) to the east, the research region displays strong local variabilities in temperature and salinity, increasing from nearshore towards the GS (Wang et al., 2018a). A strong horizontal gradient in sea surface temperature (SST) is clearly demonstrated by the data collected by the research ship’s (R/V Atlantic Explorer) SBE3S and plotted along the ship track in Fig. 1.

Meteorological observations were collected by sensors mounted on the ship’s bow mast, while the R/V remained in vicinity of the study area. These include wind speed, solar and long wave radiation, air and water temperature, and relative humidity. Time-varying wind stress, latent, and sensible heat fluxes (Fig. 2) were calculated from these data using the vectorized COARE 3.5 algorithm modified from Fairall et al. (2003) by Woods Hole Oceanographic Institution (WHOI). However, because the R/V did not always keep stationary near ASI2, the resulting time series do not cover the entire time period continuously. Thus, the U.S. Navy’s Coupled Ocean/Atmosphere Mesoscale Prediction System (COAMPS) hourly forecasts were used as atmospheric forcing for the LES model in our experiments. COAMPS is a fully coupled air–ocean modeling system that was run in real-time to support the CASPER campaign. It features a nested grid configuration with the inner grid having 2 km grid spacing distributed over 70 terrain following vertical levels. Initial and lateral boundary conditions are supplied by the Navy’s global operational models (NAVGEN for the atmosphere and HYCOM for the ocean), and every 6 h the model fields are updated with local observations. COAMPS treatment of surface fluxes follows the Louis (1979) scheme modified to obtain consistency in exchange coefficients and roughness lengths described by COARE 3.5 (Wang et al., 2002). As shown in Fig. 2, all COAMPS forcing (wind stress, latent and sensible heat fluxes, long/short wave radiation) matched well with the available observations at ASI2. More details on the model design and its performance during CASPER are provided in Ulate et al. (2019).

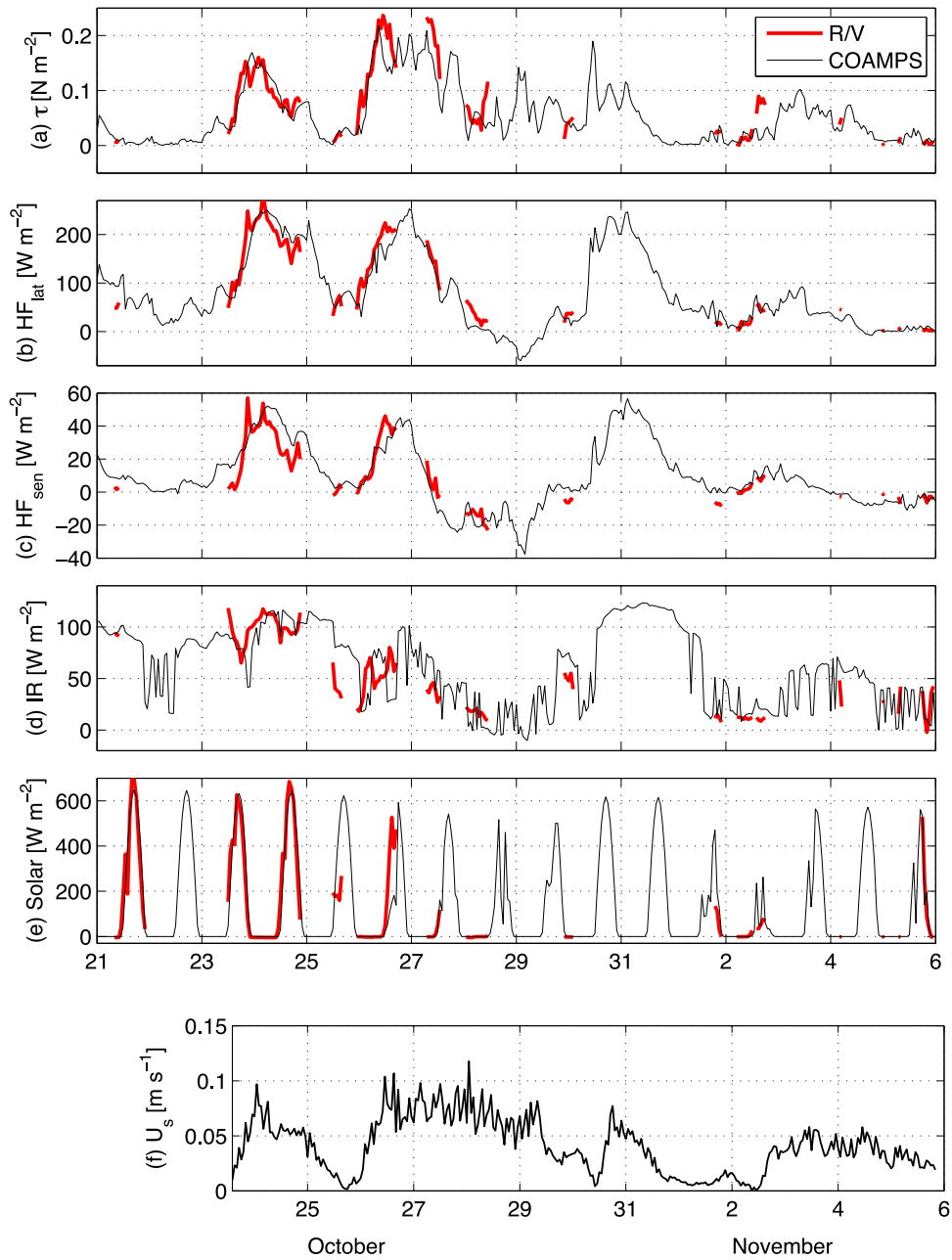


Fig. 2. Comparison of R/V observed (red) and COAMPS simulated (black) meteorology forcing for (a) wind stress  $\tau$ , (b) latent heat flux  $HF_{lat}$ , (c) sensible heat flux  $HF_{sen}$ , (d) long wave radiation IR and (e) solar radiation, and (f) surface Stokes drift  $U_s$  calculated from wave spectra collected by a Scripps miniature wave buoy (MWB) located at ASI2. Here  $\tau$ ,  $HF_{lat}$ , and  $HF_{sen}$  are calculated using the vectorized COARE 3.5 tool box.

Detailed two-dimensional wave spectra were collected by a Scripps miniature wave buoy (MWB) located at ASI2. The buoy was configured to report the directional wave spectrum at 30 min intervals. GPS 3-axis Doppler velocity time series ( $u$ ,  $v$ ,  $w$ ) were collected at a 4 Hz sampling rate, over 1024 samples (4 min, 16 s), at the beginning of each 30 min period. From these velocities, two-dimensional wave spectra were generated using the Maximum Entropy Method (Lygre and Krogstad, 1986).

A vertically profiling underwater Slocum glider with temperature, salinity, and turbulence microstructure (Rockland Scientific's MicroRider) probes was deployed to survey the area from October 19 within a short distance from ASI2 (magenta line in Fig. 1). Due to the large periods of discontinuity in the data during the first 5 days, this study only uses data starting from October 24 0UTC (Fig. 3). Large temporal temperature and salinity variations are observed along the glider track. These variations are especially striking in the surface layer where the

temperature is reduced by more than 3 degrees and salinity is reduced by almost 4 psu within a 10-day period.

## 2.2. Model description

The large eddy simulation (LES) model used for this study was first introduced by McWilliams et al. (1997) to study ocean surface boundary layer turbulence by solving the wave-phase-averaged Craik–Leibovich equations (Craik and Leibovich, 1976). The effect of surface gravity waves is included as vortex force, Stokes–Coriolis force, Lagrangian mean advection associated with Stokes drift, and a wave-averaged increment to pressure that arises through conservative wave-current interactions. The model was further improved by Sullivan et al. (2007) to include the Stokes production in the subgrid TKE equations (Appendix). It has been shown to accurately reproduce observed upper

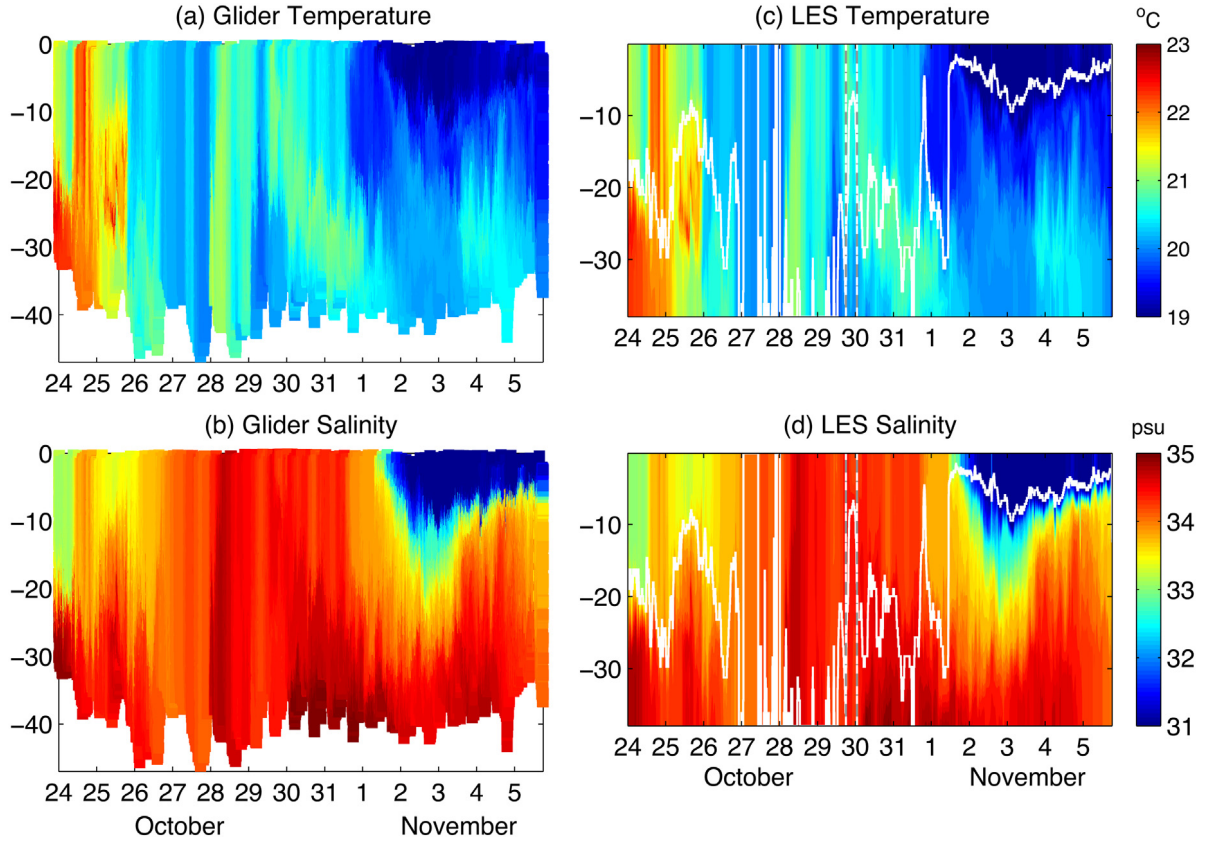


Fig. 3. Vertically profiling underwater Slocum glider measurement of vertical (a) temperature and (b) salinity v profile time series compared with LES simulated (c) temperature and (d) salinity. The white lines in (c) and (d) are mixed layer depth defined as the depth where changes of the potential density are (referenced to surface) less than  $0.1 \text{ kg/m}^3$ . The two vertical gray and white dashed lines highlight the period when total TKE is reduced with the inclusion of Stokes drift.

ocean responses to different meteorological forcing with simple ocean conditions (e.g., Kukulka et al., 2009; Liang et al., 2013, 2017).

Due to its periodic boundary conditions along the horizontal boundaries, the LES model suffers serious limitations in predicting turbulence in inhomogeneous flow fields, such as the CASPER-East research area, which displays strong spatial and temporal variabilities in temperature (T) and salinity (S). Fan et al. (2018) introduced a large-scale gradient forcing into the LES model to account for strong horizontal density gradient across the model domain and demonstrated significant improvement of model skill in simulations within a strong salinity gradient region. However, such an approach requires continuous T and S measurements at different spatial locations in order to provide the time series of horizontal T and S gradient for the LES model. Since we do not have such vast data sources from the CASPER-East field experiment, in order to account for the horizontal advection throughout the water column, T and S fields in the model are relaxed towards the glider vertical profile measurements ( $T_{obs}$  and  $S_{obs}$ ) with a relaxation e-folding time scale ( $t_{relax}$ ) of 30 min. To avoid influence of such a treatment on the small-scale turbulence in the model, we only relax the domain mean T and S towards observations as described below:

Step 1. compute the domain mean T and S vertical profile:  $\bar{T}(z)$  and  $\bar{S}(z)$

Step 2. T and S adjustments are computed using the mean values:

$$\Delta\bar{T}(z) = (T_{obs}(z) - \bar{T}(z)) * \frac{\Delta t}{t_{relax}};$$

$$\Delta\bar{S}(z) = (S_{obs}(z) - \bar{S}(z)) * \frac{\Delta t}{t_{relax}};$$

where,  $\Delta t$  is model time step.

Step 3. mean T and S adjustments are applied to each grid points (i, j) in the model domain:

$$T_{i,j}(z) = T_{i,j}(z) + \Delta\bar{T}(z); \quad S_{i,j}(z) = S_{i,j}(z) + \Delta\bar{S}(z);$$

### 2.3. Experiment set up

We focus our analysis at station ASI2 which has a water depth of 37.96 m. The LES model is configured on a domain of  $150 \text{ m} \times 150 \text{ m}$  in the horizontal and 37.96 m in vertical directions. There are 250 grid points in both horizontal directions with a uniform spacing of 0.6 m. The 64 layers of the vertical grid are stretched with a smallest spacing of 0.1 m near the surface to better resolve the boundary layer turbulence (McWilliams et al., 2014) and largest spacing of 1.8 m near the bottom. The Coriolis parameter of  $8.6077 \times 10^{-5}$  is used in the simulation corresponding to station ASI2's position at  $36.1837^\circ \text{N}$ . Periodic boundary conditions are specified for the horizontal directions, no-normal flow and specified momentum and heat fluxes are applied at the surface, and non-slip bottom boundary condition is used with roughness length of  $z_o = 0.001 \text{ m}$ . Sensitivity to model set up was tested on: grid resolution by doubling the number of points used in the vertical or horizontal direction; domain size by increasing the horizontal domain to 200 m and 300 m with the same resolution; roughness by using alternate values of  $z_o = 0.0001 \text{ m}$  and  $0.01 \text{ m}$ ; and model relaxation time scale by changing it to 1 h and 2 h. While quantitative differences were observed in certain statistics, such as the total turbulent kinetic energy or turbulent intensity, the insights and conclusions obtained in the present study were unchanged.

All model simulations start from rest. Model surface forcing of wind stress and net heat fluxes (the sum of latent and sensible heat fluxes, long/short wave radiation) are constructed using the assimilated COAMPS run. Glider measurements of temperature and salinity from October 23 at 23:58:03 UTC to October 24 at 00:01:29 were averaged in time to create the initial condition for the LES model on October 24 at 00:00 UTC. Since the location of the glider was within 4 km of ASI2 during the entire simulation period, we assume the temperature and

salinity at ASI2 is reasonably represented by the glider measurements and relax the model temperature and salinity towards the glider observations at a relaxation time scale of 30 min. Such a treatment helps to better resolve the temperature and salinity time variations at the location of interest (Fig. 3) and allows for more accurate turbulence simulations in the water column. Note that the water depth varies along the glider track within a few meters of the water depth at ASI2. The white lines on the LES results are mixed layer depth (MLD) defined as the depth where changes of the potential density (referred to surface) are less than  $0.1 \text{ kg/m}^3$ . This criterion is used for all MLD definitions in this article.

Stokes drift profile time series (Fig. 2f) were computed from the wave spectra data,  $E(f, \theta)$ , collected by the wave buoy at ASI2 according to Dean and Dalrymple (1991):

$$\bar{u}_s(z) = 2g \iint E(f, \theta) \frac{\vec{k}}{c} \frac{\cosh 2k(h+z)}{\sinh 2kh} df d\theta \quad (1)$$

where  $f$ ,  $\theta$ , and  $\vec{k}$  are the frequency, direction, and wave number vector of the spectra. The wave spectra are measured in frequency bands ranging from 0.05 to 1.95 Hz. The contribution to Stokes drift from higher frequencies were shown to be insignificant by Fan et al. (2018) and Kukulka and Harcourt (2017).

Three real case LES experiments are conducted at station ASI2 using the same ocean conditions and meteorological forcing. The only difference among these experiments is in the handling of Stokes drift. It was calculated from observed wave spectra (Eq. (1)) in experiment 1, no Stokes drift is used in experiment 2, and the observed Stokes drift is artificially aligned with the wind direction in experiment 3. Additionally, a suite of idealized experiments is conducted to illustrate the effect of wind-wave misalignment. The setup of these experiments is given in Section 3.3.

Note that observations (Gargett et al., 2004; Gargett and Wells, 2007; Kukulka et al., 2011) and large eddy simulation studies (Walker et al., 2016) in shallow water of 15–16 m depth have shown that Langmuir cells (LC) can extend throughout the whole water column. Such LCs were termed “Langmuir supercells” with crosswind scale (distance between convergence zones) three to six times the water depth. Strong near-bottom intensification of the along-wind velocity jets are typically located below downwelling regions and contribute to sediment resuspension. Tejada-Martínez and Grosch (2007) generalize the definition of shallow water to water depth equals to 1/6 of the dominant wave length, and is able to capture these “Langmuir supercells” and intensified jets near the bottom. The water depth at our study location is 37.96 m. Although it is relatively shallow, the dominant wave length is well below six times of the water depth during our research period, and our LES simulations show no velocity intensification near the bottom. Therefore, the mechanism of Langmuir supercells are not investigated in this study as we see no evidence of its existence.

### 3. Results

#### 3.1. The Turbulent Kinetic Energy (TKE) budget

The turbulent kinetic energy (TKE) budget is usually analyzed in previous studies (Grant and Belcher, 2009; McWilliams et al., 2012; Van Roekel et al., 2012) to examine the effect of LT on the mixing. The horizontal domain averaged TKE equation can be written as:

$$\frac{\partial e}{\partial t} = TurT + ShearP + BuoyP + PrsT + StokesP - \epsilon + sgs \quad (2)$$

where,

$$TurT = -\frac{1}{2} \left( \frac{\partial \langle u'^2 w' \rangle}{\partial z} + \frac{\partial \langle v'^2 w' \rangle}{\partial z} + \frac{\partial \langle w'^2 w' \rangle}{\partial z} \right) \text{ is the turbulent}$$

transport term,

$$ShearP = -\langle u' w' \rangle \cdot \frac{\partial \langle u \rangle}{\partial z} - \langle v' w' \rangle \cdot \frac{\partial \langle v \rangle}{\partial z} \text{ is the shear}$$

production term,

$$BuoyP = \alpha g \langle \theta' w' \rangle - \beta g \langle s' w' \rangle \text{ is the buoyancy production term,}$$

$$PrsT = -\frac{1}{\rho_0} \frac{\partial \langle p' w' \rangle}{\partial z} \text{ is the pressure transport term,}$$

$$StokesP = -\langle u' w' \rangle \frac{\partial u_{sx}}{\partial z} - \langle v' w' \rangle \frac{\partial u_{sy}}{\partial z} \text{ is the Stokes}$$

production term,

$e$  is the total TKE,  $\epsilon$  is the kinetic energy dissipation rate, and  $sgs$  is the subgrid-scale contribution. The angle bracket in the above equations represents horizontal domain average, the superscript prime denotes a departure from the mean value.

During most of the 11-day simulation period, the presence of Stokes drift in experiment 1 enhances the total TKE (or show comparable magnitude) relative to experiment 2 with no Stokes drift (Fig. 4), a result consistent with previous studies (Li et al., 1995; Skyllingstad and Denbo, 1995; McWilliams et al., 1997; Kukulka et al., 2009, 2010; Sullivan et al., 2012; Rabe et al., 2015). However, during a 7-hour period from October 29 18 UTC to October 30 1 UTC, a strong reduction in total TKE is observed within the mixed layer in Experiment 1 when compared with Experiment 2 (Fig. 4), contradictory to the studies mentioned earlier. This period is highlighted by the vertical gray lines and marked 0 and 1 to indicate the time instances of the event. Note that TKE is only given for 3 days in Fig. 4 so that the figure is not too busy to highlight the contradictory period.

In an idealized study, Van Roekel et al. (2012) found normalized vertical velocity variance (VVV) is less than shear-only cases in strongly misaligned ( $135^\circ$ ) wind and wave simulations, while the reduction of VVV is not observed in the studies under hurricane conditions (Sullivan et al., 2012; Rabe et al., 2015; Wang et al., 2018b, 2019) where wind-wave misalignment is common phenomenon. This is more likely due to the fact that the hurricane studies are transient, and the wind wave angle in their study only briefly reached  $135^\circ$  or larger. However, in our study, the change of wind forcing is also transient, and the wind-wave misalignment angle only ranges from  $40^\circ$  to  $90^\circ$  during period 0 to 1 (Fig. 5b), what has caused the dramatic reduction of TKE during this period?

The major term in the TKE budget (Eq. (2)) that have caused the strong reduction in total TKE during this period is found to be the shear production which is significantly reduced in experiment 1 especially in the top 2 m or so (Fig. 6a, b). Due to the effect of the Langmuir cells and the added anti-Stokes transport by Stokes–Coriolis force in the along forcing direction, the downwind velocity consequently diminishes near surface (McWilliams et al., 1997, 2012). As a result, the mean currents become more uniformly distributed with depth and thus reduces the shear production in the water column. Although Stokes production is introduced into the system in Experiment 1, the added extra term is too weak to compensate for the loss of shear production (Fig. 6d).

As noted earlier, the wind-wave misalignment angle is large during this period. Due to storm passage over the CASPER-East region, wind directions began rotating clockwise from southerlies shortly before time 0 (October 29 18 UTC) to northerlies by October 30, 08 UTC (Fig. 5a). Due to rapidly changing wind direction, the corresponding wind waves were young and less developed and the wave field was dominated by swells oriented at large angles with the wind direction, resulting in a lag of several hours before the Stokes drift and wind directions were aligned again (Fig. 5a, b, c). Note that the wind-wave angle calculated in Fig. 5b used surface Stokes direction.

However, when we align the Stokes drift through the entire water column with the wind direction and rerun the simulation in experiment 3, we see even weaker TKE in the mixed layer (Fig. 4c). While more reduction in shear production (Fig. 6c) is produced due to the further reduction of surface currents, the enhancement of Stokes production in the mixed layer is very weak (although slightly larger than experiment

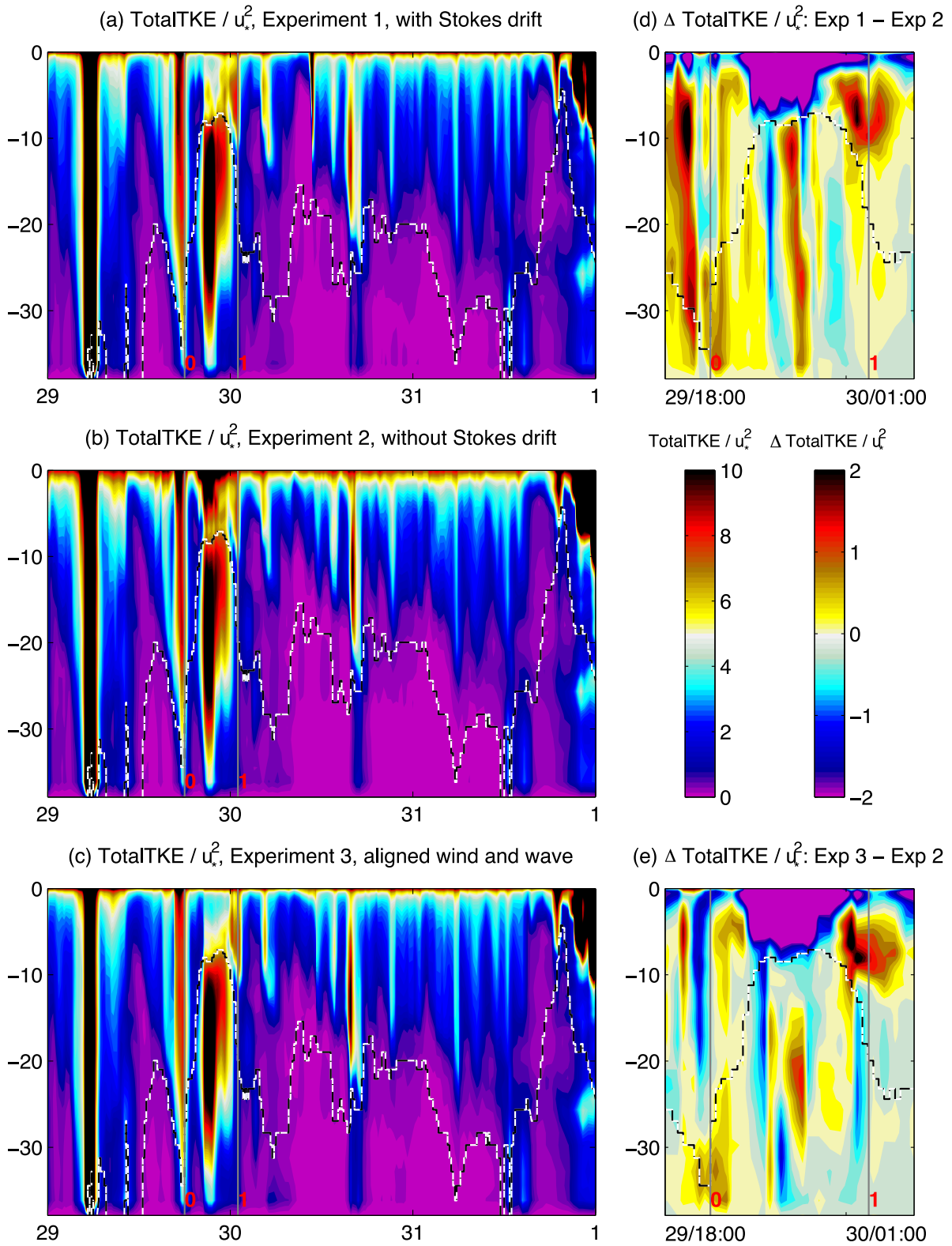


**Fig. 4.** The panels on the left show normalized turbulent kinetic energy (TKE) in (a) Experiment 1, (b) Experiment 2, and (c) Experiment 3 with the magnitude represented in the color bar on the left; The panels on the right show the normalized TKE difference between (d) Experiment 1 and 2 and (e) Experiment 3 and 2 with the magnitude represented in the color bar on the right. The black and white dashed line on the figures are mixed layer depth, and the two vertical gray lines labeled 0 and 1 indicate the period when total TKE is reduced with the inclusion of Stokes drift.

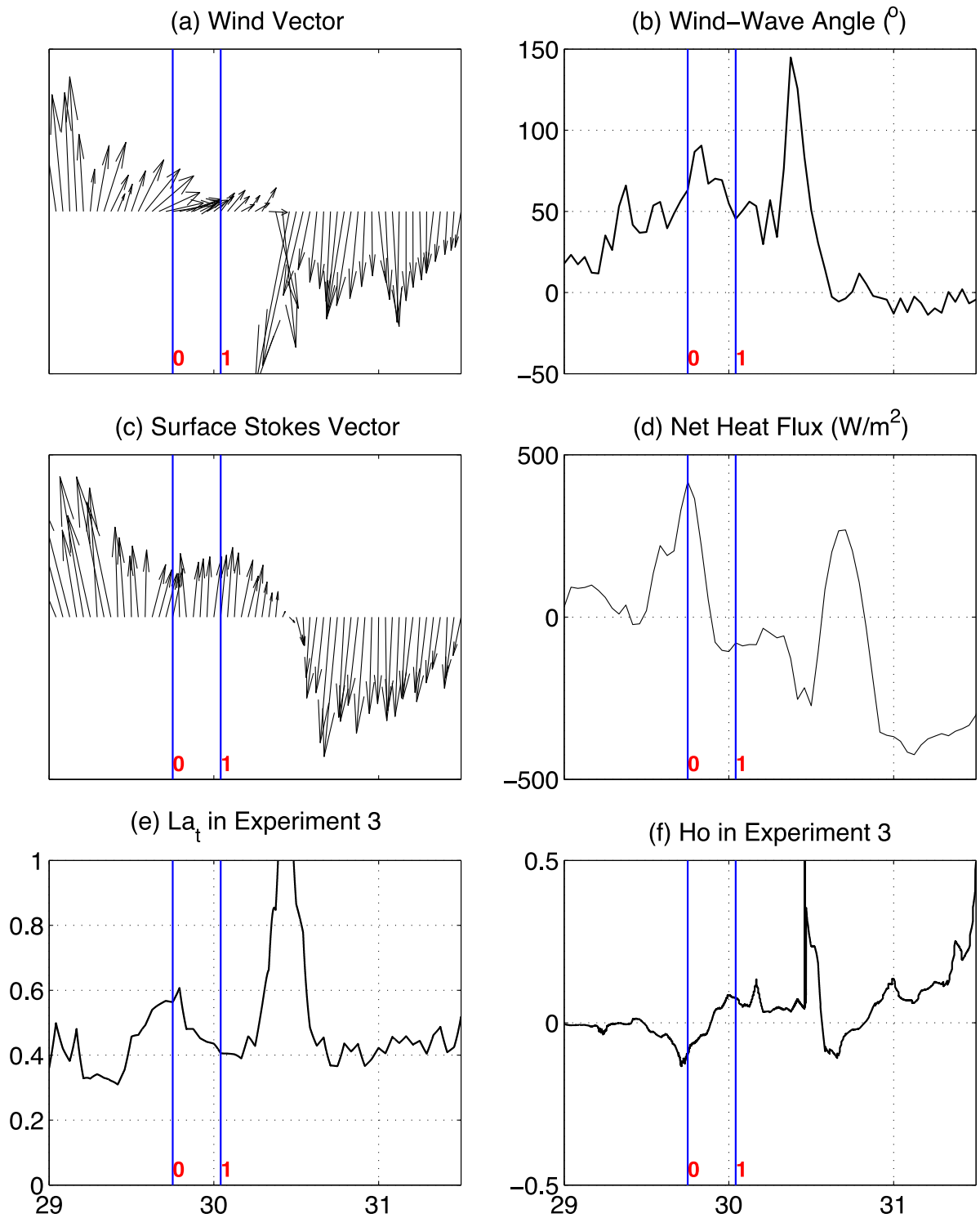


Fig. 5. Forcing variables for the LES model around the 1-day period of turbulence reduction with the inclusion of Stokes drift: (a) wind vector, (b) wind and surface wave misalignment angle, (c) surface Stokes drift vector, (d) net heat flux ( $W/m^2$ ). The (e) turbulent Langmuir number,  $La_t$ , and (f) Hoenikker number,  $Ho$  for experiment 3 are also given.

1). Thus, the total TKE in the surface layer end up to be even smaller than Experiment 1.

As we can see from Fig. 5e, unlike the previously studied idealized cases that use pure wind sea and strong Langmuir turbulence dominance with a turbulent Langmuir number,  $La_t = \sqrt{u_*}/u_s(0)$  (where  $u_*$  is the friction velocity, and  $u_s(0)$  is the surface Stokes drift), equal to 0.3, the  $La_t$  in experiment 3 ranges from 0.4 to 0.6 during this period indicating weak Langmuir turbulence. This is because although the

Stokes drift is artificially aligned with the wind directions in experiment 3, its magnitude is estimated using the observed wave spectrum. Due to the dramatic change of wind direction during this period, the growth of wind waves is small and the wave field is dominated by swells which have lower wave height and longer wave length compared with wind waves, producing smaller Stokes drift.

To further analyze the behavior of vertical mixing among these three experiments, the mixed layer averaged vertical velocity variance

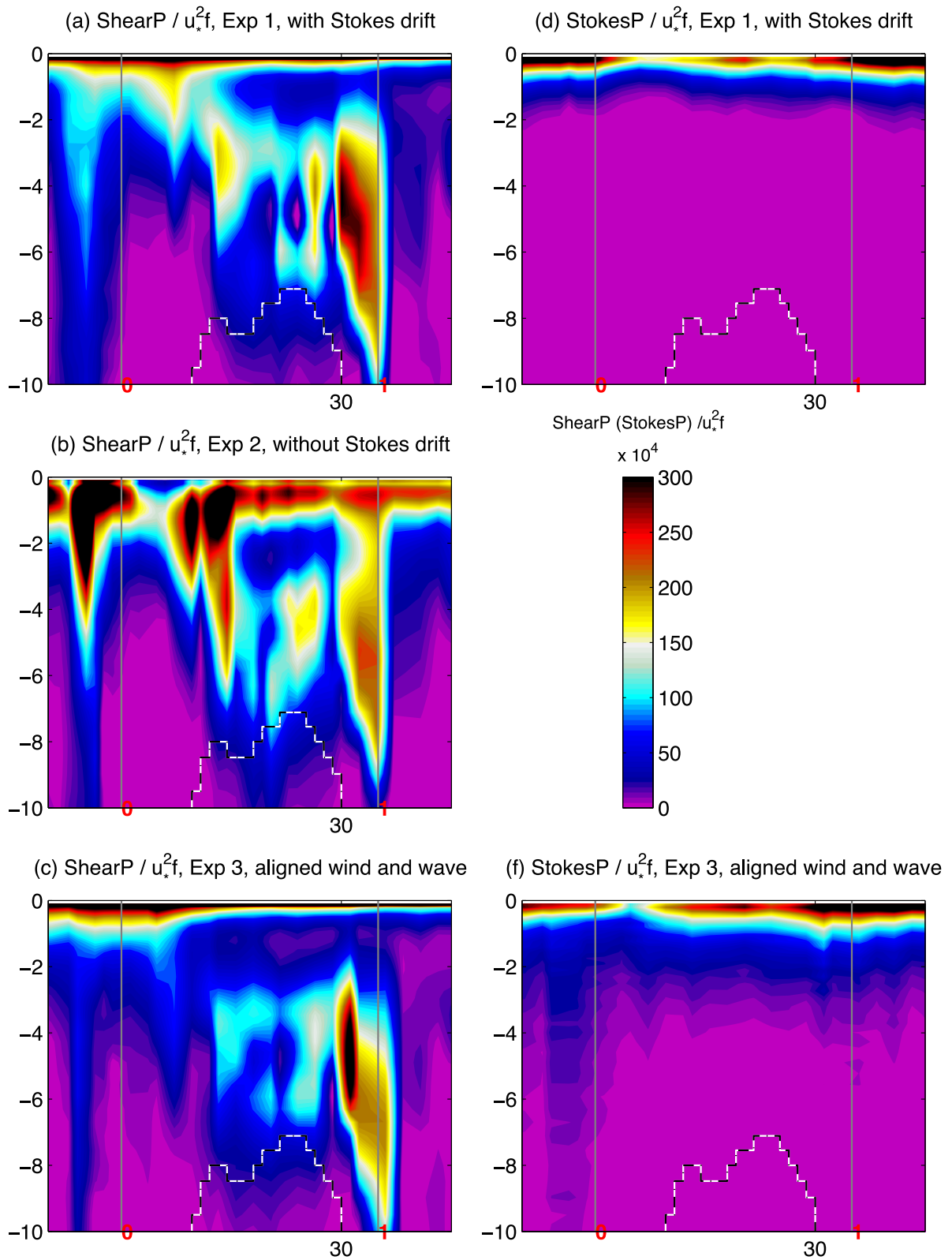


Fig. 6. The panels on the left show normalized shear production term in (a) Experiment 1, (b) Experiment 2, and (c) Experiment 3; The panels on the right show normalized Stokes production in (d) Experiment 1, and (f) Experiment 3.

(VVV) is compared in Fig. 7 for the same time period as the total TKE. According to Rabe et al. (2015), the LES bulk VVV (resolved plus SGS contribution) is calculated as

$$\langle w_T'^2 \rangle_h = \frac{1}{h} \int_{-h}^0 (\langle w'^2 \rangle + \langle w_{SGS}'^2 \rangle) dz \quad (3)$$

where  $h$  is the mixed layer depth, and subscript T represents total VVV including the subgrid-scale VVV that is calculated under the assumption of isotropic turbulence. It is defined as  $w_{SGS}'^2 = \frac{2}{3}e'$ , where  $e'$  is the subgrid-scale TKE.

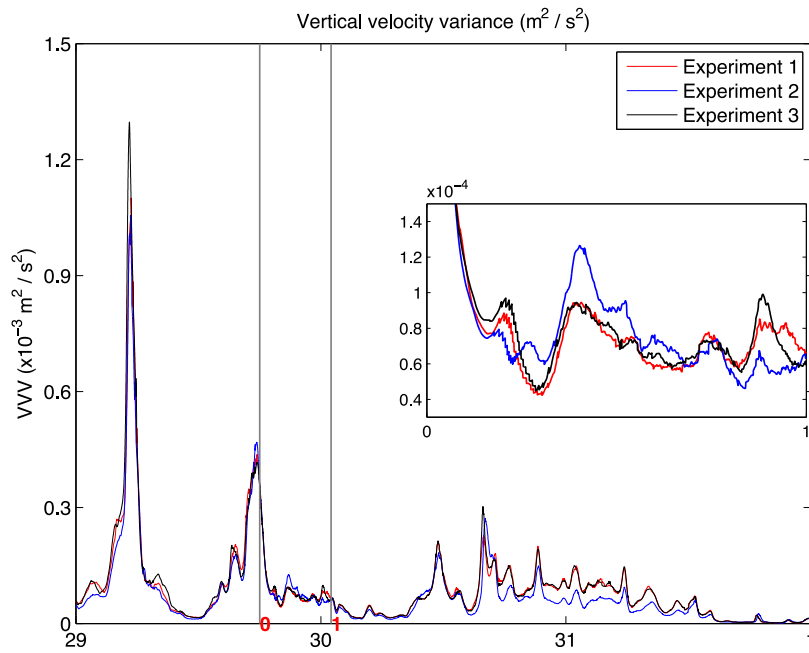


Fig. 7. Bulk VVV comparison among Experiment 1 with Stokes drift (red), Experiment 2 without Stokes drift (blue), and Experiment 3 with Stokes drift aligned with wind direction (black).

As we can see, the bulk VVV is larger in Experiment 1 than Experiment 2 during most of the simulation period, and aligning the wave direction with wind direction further enhances VVV, except for the period from 0 to 1 (enlarged in the inset figure of Fig. 7) when the bulk VVV is larger in Experiment 2 than Experiment 1 and align the waves with wind direction makes very little difference. Thus, during this period, instead of elevated VVV as shown in Rabe et al. (2015), the addition of the Craik–Leibovich vortex force reduces the vertical mixing.

From what we see in this section, it seems like that for young wind seas with swell domination, the effect of Stokes drift on reducing shear production is stronger than the Stokes production generated by the LT, and a reduction of total TKE may be expected whether or not the Stokes drift is aligned with the wind. Note that the case studied here is very different from McWilliams et al. (2014) when the authors studied the effect of very strong swells in the same direction as the fully developed wind seas, so that the turbulent field is strongly dominated by Langmuir turbulence with very small  $La_t$  (0.11–0.3). Both scenarios exist in the real ocean where the wave field is complex and fast varying with different combinations of wind seas and swells (Fan et al., 2014) created by weather patterns that constantly vary both spatially and temporally. Thus, although idealized studies can provide good insights on the effect of Langmuir turbulence, more real case studies are needed to reveal the full range of effect of Langmuir circulation in the ocean.

### 3.2. Turbulent intensity

While TKE is very informative in understanding the change of turbulence due to Langmuir circulation, ocean circulation models cannot resolve the actual turbulence due to their coarse resolutions and therefore have to parameterize it through eddy viscosity/diffusivity that relates the turbulence to the vertical gradient of resolved velocity. Thus, turbulent intensity can be an interesting variable to explore for the CASPER-East experiments. It is defined as the magnitude ratio of the velocity fluctuations ( $u', v', w'$ ) to the mean flow velocity ( $u, v, w$ ),  $I = \sqrt{\frac{\langle u'^2 \rangle + \langle v'^2 \rangle + \langle w'^2 \rangle}{3}} / \sqrt{\langle u^2 \rangle + \langle v^2 \rangle + \langle w^2 \rangle}$  (where, the angle bracket represents horizontal domain mean), and thus is a measure of the relative degree of turbulence in the fluid.

The values of the turbulent intensity from the real case LES experiments conducted at station ASI2 (experiment 1, experiment 2, and experiment 3) are compared in Fig. 8. Same as shown in the TKE comparison, the presence of Stokes drift in experiment 1 enhances the turbulence (Fig. 8a) relative to experiment 2 (Fig. 8b) during most of the 11-day simulation period except time period 0 to 1. Notice the significant differences between experiment 1 and 2 beneath the mixed layer. Since the currents in the mixed layer are much stronger than that beneath the mixed layer, and its magnitude is reduced at the same time as the total TKE reduction in experiment 1, the turbulent intensity that represents the ratio of these two shows no obvious difference between experiment 1 and 2 in the mixed layer. On the other hand, while the total TKE shows smaller differences between the two experiments beneath the mixed layer (Fig. 4d), the differences are amplified in the turbulent intensity by the small differences in the weak currents.

When we align the Stokes drift through the entire water column with the wind direction and rerun the simulation in experiment 3, the turbulent intensity in the new experiment (Fig. 8c) is significantly enhanced relative to experiment 1 indicating wind-wave misalignment may play an important role when the level of turbulence relative to the mean flow is considered.

### 3.3. The effect of wind-wave misalignment on Langmuir turbulence

A suite of idealized experiments with wind-wave misalignment angles range from 0 to 135° is conducted in Van Roekel et al. (2012) to examine the effect of wind-wave misalignment on the strength and orientation of the Langmuir cells (LC). A projected Langmuir number is suggested that takes into account of the misalignment, and an empirical formula is proposed to predict the angle between LC and wind direction. While the authors briefly noted the weakening of vertical kinetic energy ( $\langle w'^2 \rangle$ ) with the increase of wind-wave misalignment angle and found  $\langle w'^2 \rangle$  to be “only slightly different from the profiles found in the shear only case” when the mis-alignment angle is 135°, they did not examine the changes of the turbulence level relative to the mean flow or the changes of eddy viscosity in their study. Since this information is critical to ocean circulation models, a suite of idealized experiments is carried out in this section to investigate the effect of wind-wave misalignment on turbulent intensity, Reynold stress, and eddy viscosity in light of Van Roekel et al. (2012).

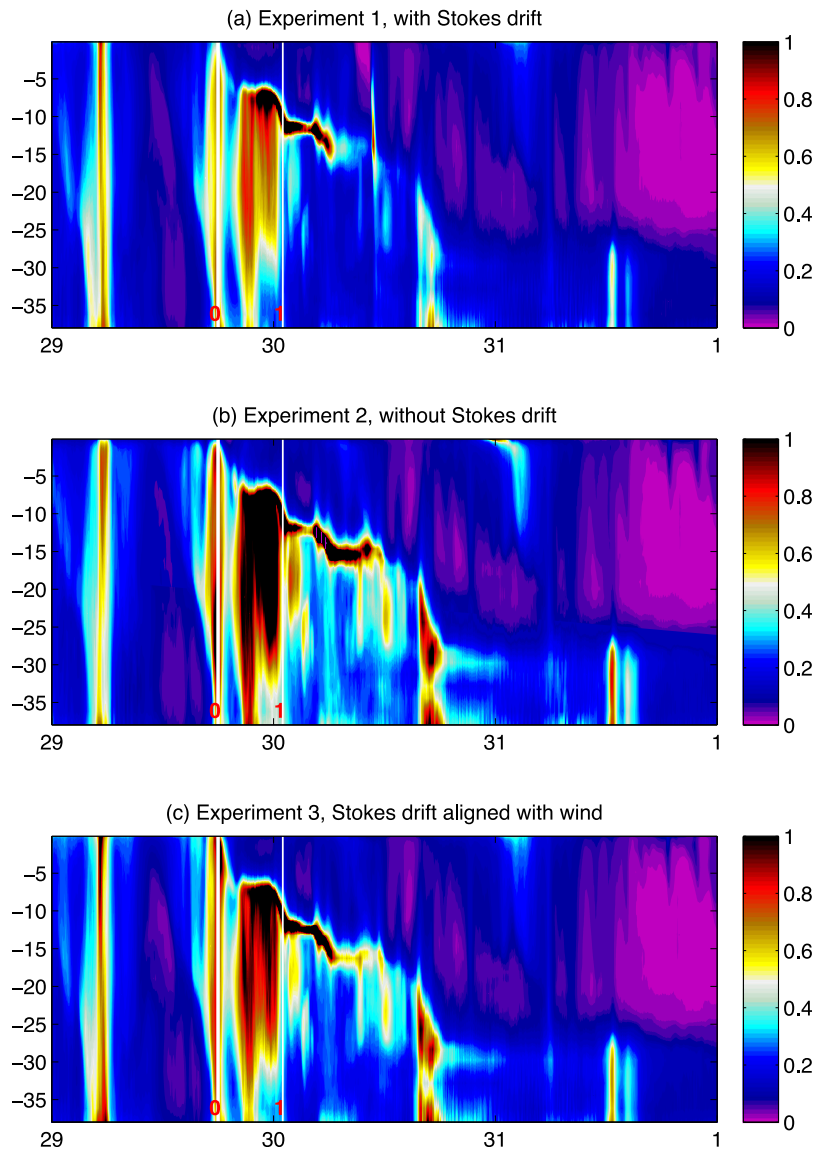


Fig. 8. LES simulated turbulent intensity defined as the magnitude of the turbulent velocity divided by the magnitude of resolved mean current ( $I = \frac{\sqrt{u'^2+v'^2+w'^2}}{\sqrt{u^2+v^2+w^2}}$ ) for (a) experiment 1 with the Stokes drift, (b) experiment 2 without the Stokes drift, and (c) experiment 3 with artificially aligned Stokes drift along the wind direction. The thin white lines indicate short research periods with reduced turbulence with the inclusion of Stokes drift.

Stratified ocean initial conditions are prescribed for the idealized experiments with a constant density layer from the surface to a depth of 20 m. Below that layer, stable stratification of  $d\theta/dz = 0.01 \text{ K/m}$  is prescribed with the thermal expansion coefficient  $\alpha = 2 \times 10^{-4} \text{ K}^{-1}$ . Constant forcing is applied for all experiments following McWilliams et al. (1997) with wind stress  $\tau = 0.037 \text{ N m}^{-2}$  (corresponding to a wind speed of about  $5 \text{ m s}^{-1}$ ), a weak heat flux into the ocean of  $Q_* = -5 \text{ W m}^{-2}$ , and a Stokes drift profile from a sinusoidal wave with an amplitude of 0.8 m and length of 60 m corresponding to Stokes drift with surface value of  $U_s = 0.068 \text{ m s}^{-1}$ . This implies a  $La_t$  equals 0.3. The  $\hat{x}$  direction in the model is defined as the along-wind direction. Seven experiments are conducted as listed in Table 1, in which the wind-wave angle,  $\theta_{ww}$ , is varied from 0 to  $120^\circ$  in  $30^\circ$  increments from experiment I1 to I5. Experiment I6 provides a reference case when no Stokes drift was present in the simulation. The boundary layer environment is uniformly rotating for all experiments, with  $f = 8.5867 \times 10^{-5} \text{ s}^{-1}$ , corresponding to  $36.17^\circ \text{ N}$  latitude (the latitude of station ASI2). All model runs are spun up from rest to a statistical equilibrium state after one inertial period ( $\sim 20.3 \text{ h}$ ).

Turbulent intensity time series for two days of model simulation are presented in Fig. 9 after the first day of model simulation to exclude the

Table 1  
Idealized experiment set up, where  $\theta_{ww}$  represents the wind-wave angle.

Experiments	I1	I2	I3	I4	I5	I6
$\theta_{ww} (^\circ)$	0	30	60	90	120	–
Stokes drift	Yes	Yes	Yes	Yes	Yes	No

turbulence spin up period. We note that the turbulence is the strongest with deepest reach when wind and wave is aligned (experiment I1) and it gives the largest averaged MLD of 33 m during this period, while the case without the Stokes drift (experiment I6) has weaker turbulence and shallower MLD of 28.2 m, consistent with previous studies. Note, the large values of turbulent intensity (red areas) beneath the mixed layer is an artifact caused by the extremely small mean current there.

Consistent reduction of turbulence in the water column is observed as  $\theta_{ww}$  gradually increases from 0 to  $120^\circ$  (experiment I1 to I5). Not only does the magnitude of turbulent intensity decrease, but it is confined to an increasingly shallower layer near the surface. Even when the winds and waves are misaligned by only  $30^\circ$  (experiment I2, Fig. 9b), the magnitude of the turbulent intensity with the presence

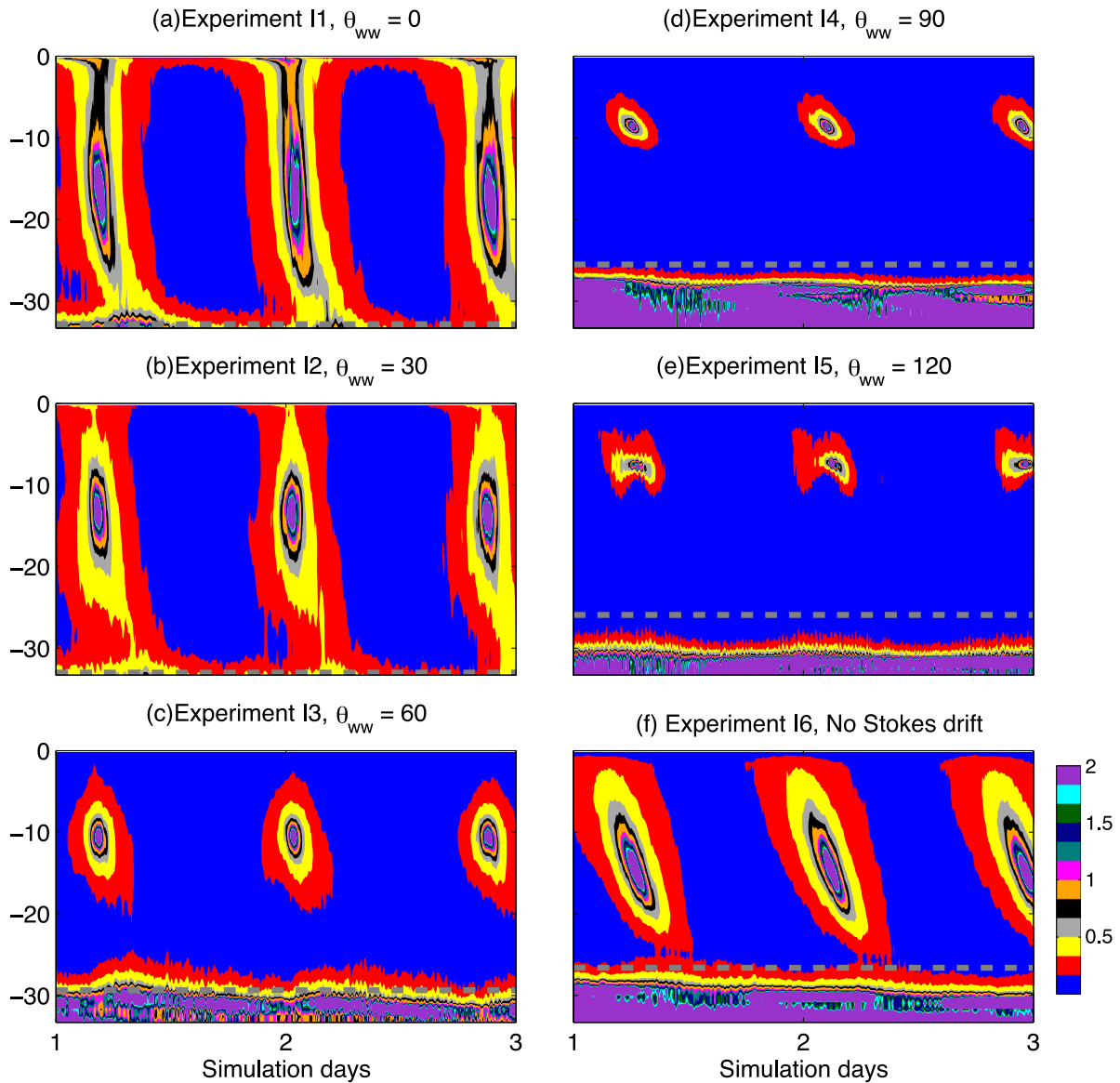


Fig. 9. Turbulent intensity for idealized cases.

of Stokes drift is already comparable to the case without Stokes drift, although it still gives a deeper mixed layer. The reduction of turbulence in the water column results in shallower MLD with increasing  $\theta_{ww}$ . Case I3, with  $\theta_{ww} = 60^\circ$  gives a comparable MLD as with no Stokes drift, while further increase in  $\theta_{ww}$  gives shallower MLD than case I6 without Stokes drift.

Another set of experiments were conducted using the same ocean conditions and heat flux but with a stronger wind speed of  $10 \text{ m s}^{-1}$  and a corresponding Stokes drift velocity of  $0.135 \text{ m/s}$ , which also implies  $La_t$  of  $0.3$ . The same trend of decreasing turbulence intensity with increasing wind-wave angle is observed. However, there is stronger turbulence in the water column for  $\theta_{ww} = 30^\circ$  when compared with the no Stokes drift case. This suggests that both the magnitude of the winds and waves, and their misalignment angle are important for the impact of Stokes drift on the level of turbulence intensity when other conditions are kept the same. This difference should not be expected with carefully designed experiments when all controlling non-dimensional variables are kept constant.

To quantify the significance of wind-wave misalignment on ocean models, we diagnose the scalar eddy viscosity magnitude  $K_m$  obtained from the Reynolds stress and mean shear following McWilliams et al.

(2012):

$$K_m = \frac{|\langle u'w \rangle|}{|\partial_z \langle u^L \rangle|} \quad (4)$$

where  $\langle u'w \rangle$  is the horizontal domain averaged total Reynolds stress, and  $\langle u^L \rangle$  is the horizontal domain averaged Lagrangian velocity (mean current plus Stokes drift).

Fig. 10 shows the bulk eddy viscosity for all 6 experiments. All statistics presented here are averaged over one inertial period (20.3 h) towards the end of the simulation. Averaging over alternate inertial periods, or several inertial periods were tested and showed no statistical difference. As suggested by previous studies (McWilliams et al., 1997), when the Stokes drift is aligned with the wind directions (experiment I1, red solid line),  $K_m$  takes a convex profile shape and is significantly larger than the case without Stokes drift (experiment I6, black solid line). When the Stokes drift direction is rotated away from the wind direction, the magnitude of  $K_m$  is reduced. Although LT still significantly enhances  $K_m$  with a  $30^\circ$  wind-wave misalignment angle, on average it adds no apparent turbulence to the water column for a  $60^\circ$  angle, and even reduces  $K_m$  when the misalignment angle is further increased.

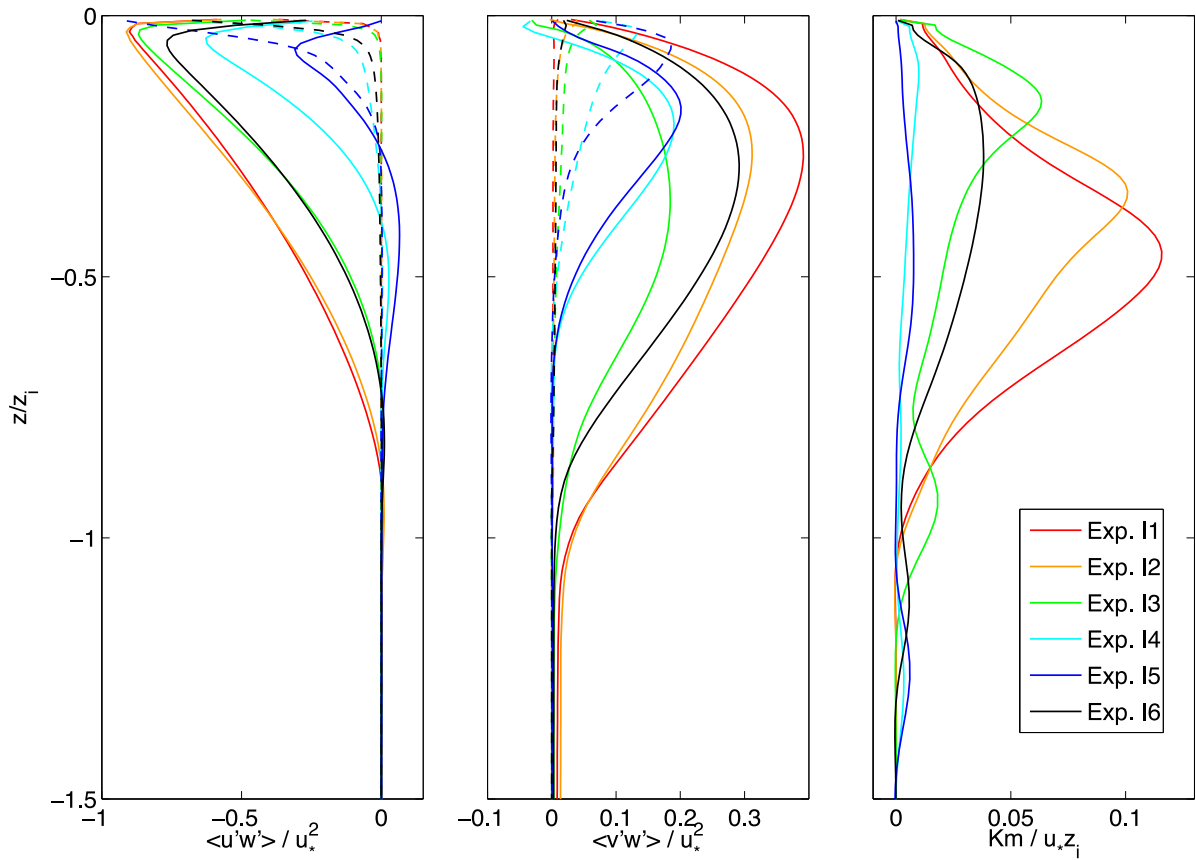


Fig. 10. Resolved (solid lines) and subgrid scale (dashed line) turbulent vertical Reynolds stress (a)  $\langle u'w' \rangle$  and (b)  $\langle v'w' \rangle$  normalized by  $u_*^2$ . (c) Bulk eddy viscosity profiles normalized by  $u_*$  and averaged mixed layer depth  $z_i$ .

In the along wind direction ( $x$ -direction), the structure of the resolved Reynolds stress,  $\langle u'w' \rangle$ , profiles look qualitatively similar for all cases with significant magnitude and penetration depth differences (Fig. 10a, solid lines). When the wind-wave angle is relatively small (up to  $30^\circ$ ), the LT enhances the magnitude of the Reynolds stress with deeper penetration in the interior of the boundary layer compared with the shear turbulence only case (experiment I6). The LT can still lead to higher magnitude of  $\langle u'w' \rangle$  when  $\theta_{ww}$  reaches 60 degrees, but the penetration depth becomes the same as the non-Stokes case. Further increase of  $\theta_{ww}$  leads to a significant decrease in both the magnitude and penetration depth of the resolved momentum flux.

Since the subgrid scale (SGS) part of the momentum flux (given in Appendix) is a function of the strain tensor, its vertical profiles are strongly dependent on the vertical shear of the resolved velocity components which are given in Fig. 11. The magnitude of both the along and cross wind Eulerian velocities increase sharply with  $\theta_{ww}$ , become increasingly confined to the surface layer, and their vertical shear significantly overwhelms the vertical shear from the Stokes drift. Thus, the maximum values of the SGS momentum flux in the along wind direction are found near surface where the strongest mean velocity shear is located, and increase significantly with the increase of  $\theta_{ww}$ . The penetration depth of the SGS momentum flux also increases significantly with the increase of  $\theta_{ww}$  from very close to the water surface when the wind-wave misalignment is within  $60^\circ$  to 20% of the total boundary layer depth when  $\theta_{ww}$  reaches  $120^\circ$ . Note that when  $\theta_{ww}$  reaches  $120^\circ$ , the SGS portion exceeds the resolved portion of the total momentum flux in the upper boundary layer, thus indicating the flow regime becomes dominated more by small scale motion, and that the LES solutions are more sensitive to the SGS models used.

In the cross-wind direction ( $y$ -direction), the structure of the resolved Reynolds stress,  $\langle v'w' \rangle$ , profiles also look qualitatively similar for

all cases with significant magnitude and penetration depth reductions due to the increase of  $\theta_{ww}$  (Fig. 10b). However, when  $\theta_{ww}$  reaches  $60^\circ$ , the magnitude of the resolved momentum flux becomes much smaller than the case without Stokes drift. While the magnitude of the resolved momentum flux continues to reduce with the increase of  $\theta_{ww}$ , the level of reduction is weaker compared with the along wind component.

While the cross-wind SGS momentum fluxes appear to have their maximum values at the surface as the along wind components when  $\theta_{ww}$  is less than  $90^\circ$ , the profiles start to show a convex shape structure when  $\theta_{ww}$  is equal to or larger than  $90^\circ$ . The maximum of the fluxes is found below the surface, and it becomes deeper with a larger magnitude as  $\theta_{ww}$  further increases. This is owing to the slight curvature in the mean cross-wind velocity  $v$  near the surface (Fig. 11b) that reduces the vertical shear.

The wind-wave misalignment directly impacts both the resolved and subgrid-scale energy since their balance equation includes a Stokes production term. Van Roekel et al. (2012) studied the effect of misalignment on the TKE budget in detail, and found that the primary balance within the TKE budget is between Stokes shear production and the SGS terms, and it undergoes significant changes as  $\theta_{ww}$  increases. For small  $\theta_{ww}$ , the primary balance is between the Stokes shear production in the along wind direction and the SGS terms. As  $\theta_{ww}$  increases, the Stokes shear decreases in along wind direction while increases slowly in the cross-wind direction. Our model results are consistent with these findings and thus not shown here.

Note that Pearson (2018) showed that the use of SGS model in LES simulation with Stokes drift leads to an artificial TKE production close to the surface when the wind-wave angle is close to  $90^\circ$  at the equator. Since our simulation is conducted at mid-latitude ( $36.1837^\circ\text{N}$ ), that effect is likely minimal.

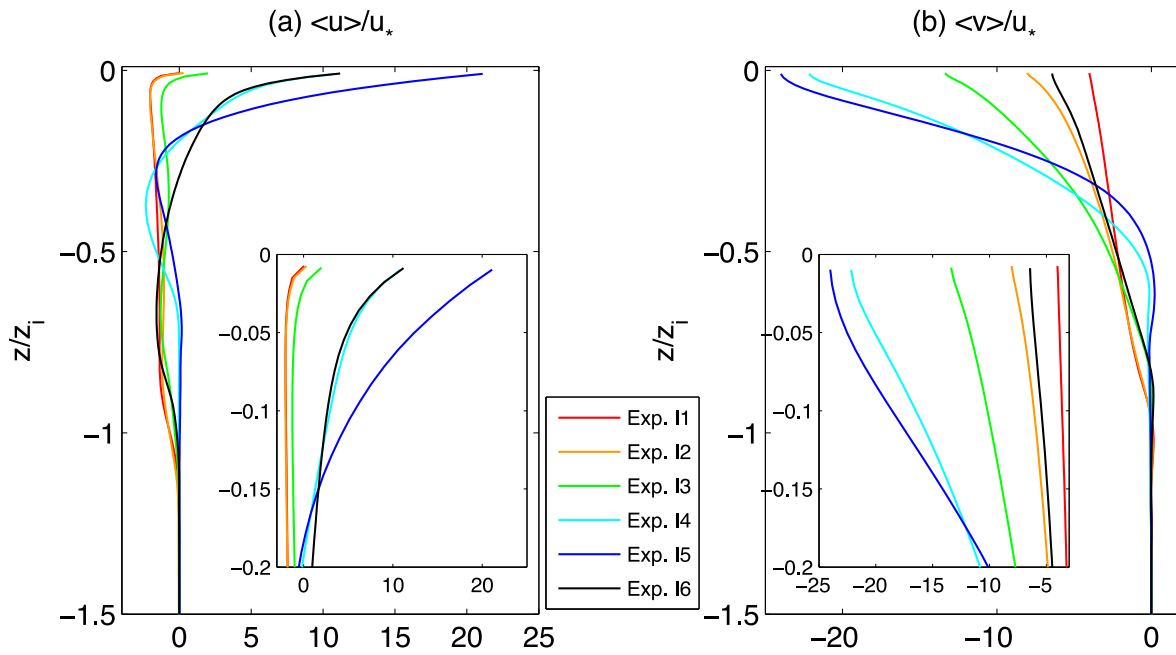


Fig. 11. Mean velocity profile for idealized case with uniform density. Different color represent different experiment as indicated in the legend.

#### 3.4. Interaction between Langmuir turbulence and deep convection

In the real case simulations at station ASI2 (discussed in Sections 3.1 and 3.2), during a 7-hour period from October 29 18 UTC to October 30 1 UTC, we not only observed a strong reduction of TKE in the mixed layer due to the inclusion of Stokes drift in experiment 1 (Fig. 4a) but also noticed reduction of TKE beneath the mixed layer (Fig. 4d). This reduction of TKE beneath the mixed layer became stronger after we aligned the wind and waves in experiment 3 (Fig. 4e).

As discussed in Section 3.1, although the Stokes drift is artificially aligned with the wind directions in experiment 3, its magnitude is smaller than fully developed wind seas due to young under-developed wind waves and swell dominance in the wave field. Thus, the turbulent Langmuir number,  $La_t$  is large (0.4–1) in experiment 3 (Fig. 5e). While the Hoenikker number  $Ho = 4B_0/u_s\beta u_*^2$  (where  $B_0$  is the surface buoyancy flux, and  $\beta$  is the Stokes drift current e-folding depth) is still less than 1 (the critical value for transition from LT to convective turbulence, Min and Noh, 2004; Li et al., 2005), its magnitude (Fig. 5f) is much larger than typical values of  $O(0.01)$  found in idealized experiments dominated by LT (Li et al., 2005). Thus, both metrics suggest a turbulence regime with combined LT and convective plumes at the ASI2 research site.

Several hours before time 0 (October 29 18 UTC), there is an intrusion of warmer and saltier water in the upper layers (Fig. 3) that has increased the density of the surface water and reduced the mixed layer depth with heavier water overlay on lighter water (Fig. 12a). While the unstable structure has led to active turbulent mixing to efficiently mix this dense water downward and deepen the mixed layer by time 0, the continuous intrusion of warmer and saltier water together with the strong cooling event that starts at time 0 (Fig. 5d) has significantly increased the density in the surface water and reduced the mixed layer depth to just 5–7 m. Although some fresher water was introduced to the system a few hours later (Fig. 3) that has reduced the density of the surface water (Fig. 12a), another intrusion of saltier water together with strong cooling event a few hours later densifies the surface water and shallows the mixed layer again. We can clearly see these heavy waters propagate down the water column in Fig. 12a.

Notice that the event with lower turbulent intensity in the Langmuir case (experiment 1 and 3) happens beneath the mixed layer and coincide with joint events of mixed layer shallowing due to warmer

and saltier water inflow and the surface cooling caused by meteorology events. We compare the model results between experiment 2 and 3 in Fig. 13 to unveil the effect of LT during these cooling events by taking a close look at the magnitude of the vertical turbulent velocity,  $w'$ , and the vertical velocity skewness following McWilliams et al. (1997) definition:

$$\gamma = \frac{\langle w^3 \rangle}{\langle w^2 \rangle^{3/2}} \quad (5)$$

where the angle brackets represent the horizontal domain average.

##### From time 0 to time 1

The intrusion of warmer and saltier water together with the strong cooling event that starts at time 0 (Fig. 5d) has significantly increased the density in the surface water and reduced the mixed layer depth to just 5–7 m. While this dense water is mixed down the water column, fresher water inflow (Fig. 3) has created a light layer near surface, and a dense layer end up sandwiched in between of two light layers (Fig. 12a).

A prominent feature during this period is the strong vertical velocity  $w'$  beneath the mixed layer, which is associated with large negative  $\gamma$  values for both experiments 2 and 3 (Fig. 13). According to Sullivan et al. (2007), negative values of  $\gamma$  are indicative of strong short-lived downwelling events alternating with weaker longer-lived upwelling events, and can thus be used to indicate the presence of Langmuir circulation or unstable convection. Since the  $w'$  values are much weaker in the mixed layer, and there is heavy water at a depth of  $\sim 5$  m overlay on lighter water in the water column (Fig. 12), the large  $w'$  values beneath the mixed layer have to be associated with deep convection plumes.

Notice that the heavy water near the base of the mixed layer (light orange color) is thicker in Experiment 3 (Fig. 12c) compared with Experiment 2 (Fig. 12b). Since the TKE in Experiment 2 is much stronger than Experiment 3 in the mixed layer (Fig. 4), it is natural to think that the enhanced TKE has led to the thinner layer of heavy water in Experiment 2. However, enhanced TKE in the mixed layer should erode the part of the heavier water above the mixed layer base, not below as we observed in Fig. 12. Thus, another explanation is attempted here on the interaction between Langmuir circulation and deep convection.

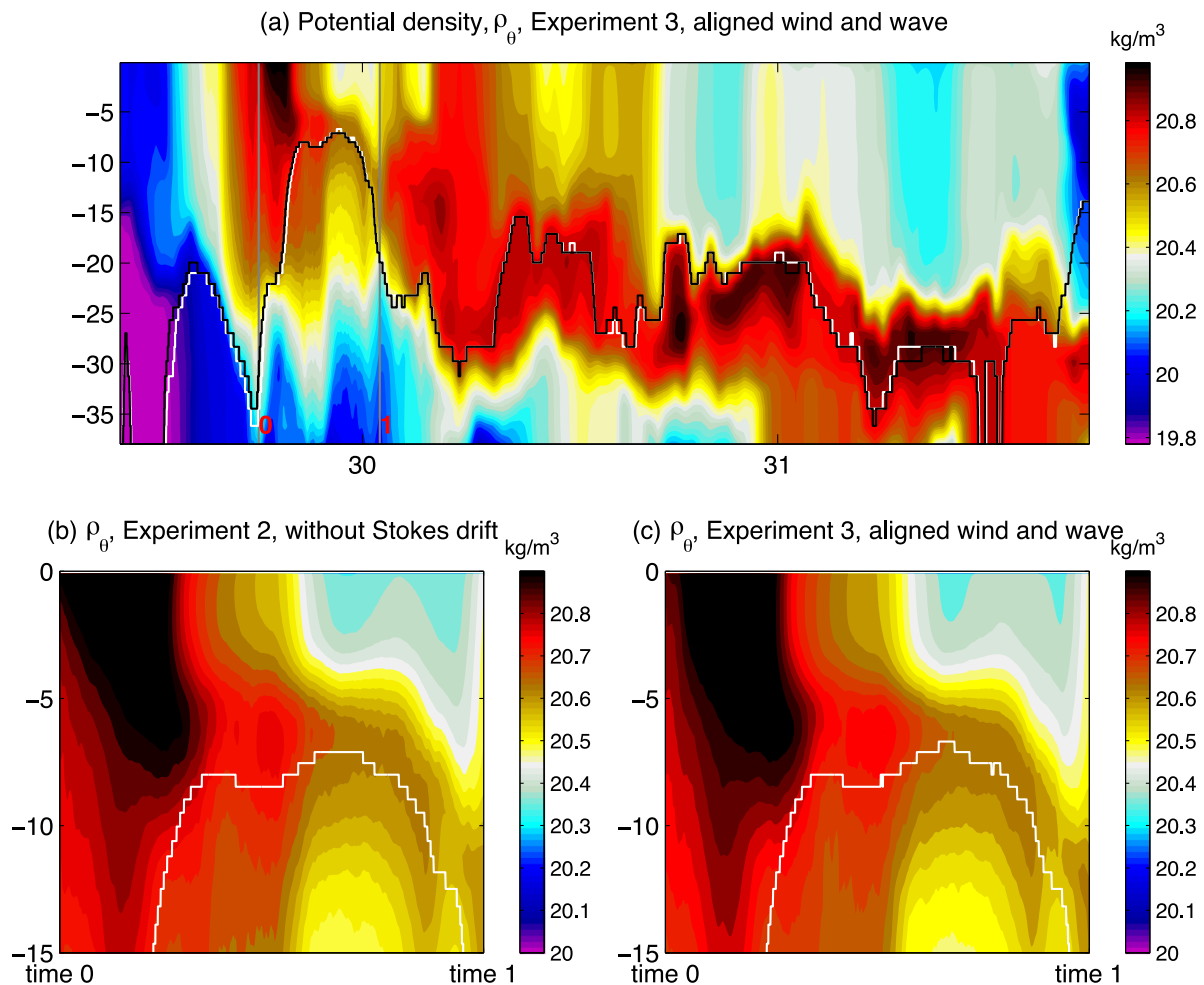


Fig. 12. (a) Potential density  $\rho_\theta$  for experiment 3 around the 1-day period with turbulent reduction for the case with Stokes drift. The comparison of  $\rho_\theta$  between (b) experiment 2 and (c) experiment 3 from time 0 to 1 given for the top 15 m.

At the base of the mixed layer, we observe reduced  $w'$  near the base of the mixed layer and below the mixed layer depth associated with reduced magnitude in negative  $\gamma$  in Experiment 3, indicating weaker convection plumes. What happens here could be that the well-organized upwelling associated with Langmuir cells has weakened the downward propagation of the denser water (weaker  $w'$  around the base of the mixed layer in experiment 3, Fig. 13c) and lead to a thicker dense water layer below and above lighter water at the base of the mixed layer in experiment 3 compared with experiment 2 (Fig. 12c and b). Since the enhanced upwelling is counter acting on the downwelling associated with the deep convection beneath the mixed layer, it reduced the overall turbulence level beneath the mixed layer.

#### 4. Summary and discussions

Langmuir turbulence (LT) is believed to be one of the leading causes of turbulent mixing in the upper ocean (Li et al., 1995; Skyllingstad and Denbo, 1995; Kukulka et al., 2009, 2010; McWilliams et al., 1997; Hamlington et al., 2014). Large eddy simulation (LES) models that solve the Craik–Leibovich equations are used to study LT, yielding new insights that could not be obtained from field observations or turbulent closure models alone. However, these studies have been mostly conducted under idealized conditions.

In this study, we expand our previous LES modeling investigations of LT to the real ocean with complex oceanic and meteorological conditions. Data collected through a multi-platform field campaign, “Coupled Air–Sea Processes and Electromagnetic (EM) ducting Research

(CASPER-East)” are used for the LES simulations. This ONR-funded field study took place off the coast of North Carolina in late October to early November of 2015. The study area is constantly influenced by inflows of fresher and colder water from nearby rivers and bays, and warmer and saltier water along the Gulf Stream, and experienced several cooling events and dramatic turning of wind directions due to a passing storm during the observation period. Ocean temperature (T), salinity (S) and directional surface gravity wave spectrum were collected together with atmospheric measurements, providing a rich data set to study the effects of LT on the dynamics and structure of the oceanic mixed layer under complicated oceanic and meteorological conditions.

In order to account for the effect of strong local variability in T and S while restricted to periodic horizontal boundary conditions, model T and S are relaxed toward glider measurements with a relaxation e-folding time scale of 30 min. The Stokes drift profile time series were computed from the two-dimensional wave spectra collected by a Scripps miniature wave buoy (MWB) located at station ASI2, and temporally evolving atmospheric forcing was provided from hourly forecasts using the COAMPS coupled mesoscale model.

During most of the simulation period, LT enhances the turbulence in the water column and deepens the mixed layer, being consistent with previous studies (Li et al., 1995; Kukulka et al., 2009, 2010; Skyllingstad and Denbo, 1995; McWilliams et al., 1997; Hamlington et al., 2014). However, significant reduction in turbulent kinetic energy (TKE) and

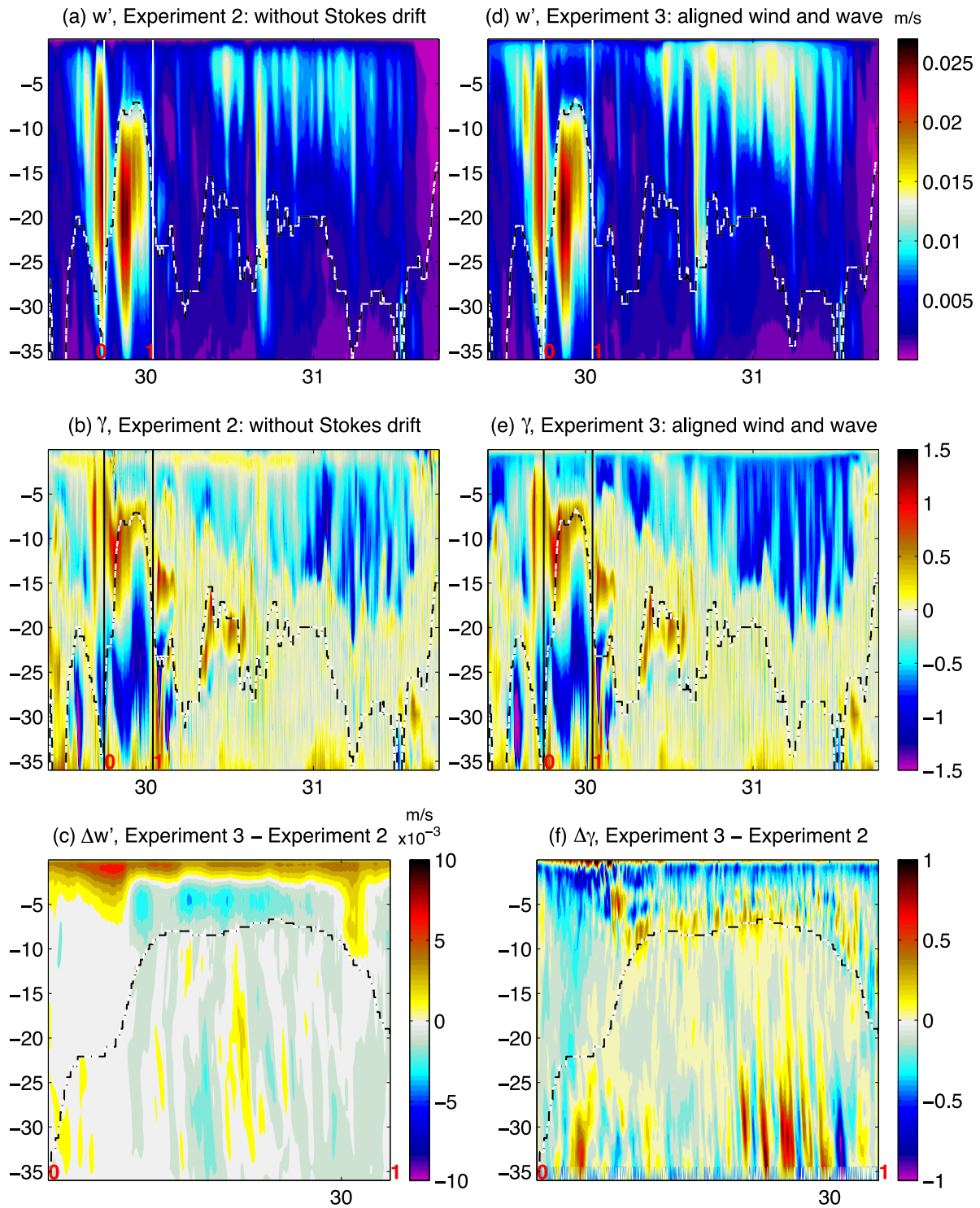


Fig. 13. (a) Magnitude of vertical turbulent velocity  $w'$  and (b) vertical velocity skewness  $\gamma$  in experiment 2 compared with (d) Vertical turbulent velocity  $w'$  and (e) vertical velocity skewness  $\gamma$  in experiment 3, and the differences between Experiment 3 and 2 for (c)  $w'$  and (f)  $\gamma$  around the 7-hour period with turbulence reduction due to the inclusion of Stokes drift in the LES simulation.

turbulent intensity ( $I = \sqrt{\frac{\langle u'^2 \rangle + \langle v'^2 \rangle + \langle w'^2 \rangle}{3}} / \sqrt{\langle u^2 \rangle + \langle v^2 \rangle + \langle w^2 \rangle}$ ) are observed in the simulation with Stokes drift compared to one without during a short period, contradicting the commonly accepted concept that LT significantly enhances turbulent mixing in the water column.

Analysis of the meteorology forcing and the TKE budget have revealed that in the circumstance of swell dominated wave fields with

young under-developed wind seas, the effect of Stokes drift on reducing shear production is stronger than the Stokes production generated by the LT, and a reduction of total TKE may be expected whether or not the Stokes drift is aligned with the wind. Since the ocean waves are complex and fast varying with different combinations of wind seas and swells created by weather patterns that constantly vary both spatially and temporally, both the wave condition studied here and the scenario

that consists of very strong swells in the same direction as the fully developed wind seas studied in McWilliams et al. (2014) exist in the real ocean. Thus, while idealized studies are good tools for us to gain more understanding of the effect of Langmuir turbulence, conducting real case studies are critical to reveal the full range of effect of Langmuir circulation in the ocean.

A suite of idealized experiments is conducted to investigate the effect of wind-wave misalignment angle,  $\theta_{ww}$  on LT. Consistent reduction of turbulent intensity in the water column and shallowing of the mixed layer depth is observed with the increase of  $\theta_{ww}$ . The wind-wave misalignment also traps the momentum in a shallower surface layer, thus producing large mean surface currents leading to a further reduction in the turbulent intensity. Both the magnitude of the wind and waves, and their misalignment angle are found to be important for the impact of Stokes drift on the level of turbulence in the water column.

While both resolved Reynold stresses in the along and cross-wind directions and the bulk eddy viscosity decrease with an increase in  $\theta_{ww}$ , the subgrid scale (SGS) part of the momentum flux increases with the increase of  $\theta_{ww}$ . This is because the SGS momentum flux is a function of the strain tensor. Its vertical profiles are strongly dependent on the vertical shear of the resolved velocity components which sharply increase with  $\theta_{ww}$  in the near surface layer in both along and cross-wind directions. The model results also suggest that the turbulence regime becomes dominated more by small scale motion with increasing  $\theta_{ww}$ , and thus suggesting that the LES solutions in cases with large wind-wave misalignment become more sensitive to the SGS models used. When Stokes drift has a component in the opposite direction of the wind, it creates a sink term for the TKE and affect the sub-grid scale turbulence behavior in the stable boundary layer in a way that is not very well understood. Thus, we recommend caution in interpolating these results and more detailed studies are needed to gain full confidence on the sub-grid model in large wind-wave misaligned cases.

In the CASPER-East simulations, reduction of turbulence due to the presence of surface gravity waves are also found during a cooling event that coincide with the intrusion of warmer and saltier water by the Gulf stream. These changes of environmental conditions have led to a special dynamical structure in the water column with a layer of denser water sandwiched in between of two layers of light water. A possible explanation could be that the well-organized upwelling associated with Langmuir cells weakens the downward propagation of the denser water and thus creates a thicker density barrier at the base of the mixed layer compared to the non LT case. The enhanced upwelling due to LT has reduced the occurrence of deep convection beneath the mixed layer and consequently reduces the overall turbulence in the water column. Although this type of density structure in the water column is not commonly observed, it demonstrates one of the complexities encountered in the real ocean resulting from nonlinear interactions between LT and dynamical processes that have been absent in previous idealized LES modeling studies.

Although many ocean models simulate temperature and salinity profiles nowadays, correct representation of the dynamics is still needed to obtain accurate turbulence in the water column. As demonstrated by these CAPSER-East simulations, even if the model relaxes its temperature and salinity towards observations, the turbulence in the water column is still very different with and without the presence of surface gravity waves. Since available ocean observations are very limited both spatially and temporally, good representation of the turbulence in the water column is still critical for ocean models, especially for the transfer of heat, momentum, and gas within the oceanic boundary layer. Better understanding of the nonlinear interaction between LT and complicated ocean dynamics and meteorological forcing is needed to correctly represent their effects on ocean turbulence.

#### Declaration of competing interest

The authors declare that they have no known competing financial interests or personal relationships that could have appeared to influence the work reported in this paper.

#### Acknowledgments

The authors thank Dr. Adam Christman for providing the R/V air-sea flux data for this study. This work was funded by the Office of Naval Research, United States of America under program element 0601153N. This paper is a contribution of NRL/JA/7320-19-4508 and has been approved for public release. We would like to express our appreciation to the anonymous reviewers for their constructive comments. Observations presented in the manuscript are open-access data. Please contact Dr. Ivan Savelyev for accessing the data ([ivan.savelyev@nrl.navy.mil](mailto:ivan.savelyev@nrl.navy.mil)).

#### Appendix. The Subgrid Scale (SGS) model

The SGS model in the NCAR LES model is originally developed by Moeng (1984). It takes the same form as Eq. (2) except the fluxes are parameterized instead of being resolved. The prognostic equation for the subgrid scale (SGS) turbulent kinetic energy (TKE)  $e'$  is given as:

$$\frac{\partial e'}{\partial t} + \bar{\mathbf{u}} \cdot \nabla e' = P' + B' + D' - \epsilon' \quad (\text{A.1})$$

where  $\bar{\mathbf{u}}$  is the resolved velocity vector, the terms on the right side are subgrid-scale production ( $P'$ ), buoyancy ( $B'$ ), diffusion ( $D'$ ), and dissipation  $\epsilon'$ :

$$P' = -\tau'_{ij} S_{ij} \quad (\text{A.2})$$

with the strain tensor:  $S_{ij} = \frac{1}{2} \left( \frac{\partial u_i}{\partial x_j} + \frac{\partial u_j}{\partial x_i} \right)$   
and the SGS momentum flux (stress):  $\tau'_{ij} = -2\nu_t S_{ij}$

$$B' = -\nu_\theta \frac{g}{\theta_0} \frac{\partial \theta}{\partial x_i} \quad (\text{A.3})$$

$$D' = \frac{\partial}{\partial x_i} \left( 2\nu_t \frac{\partial e}{\partial x_i} \right) \quad (\text{A.4})$$

$$\epsilon' = \frac{C e^{3/2}}{l} \quad (\text{A.5})$$

In the above equations,  $\theta$  is heat,  $\nu_t$  is the SGS turbulent eddy viscosity,  $\nu_\theta$  is the SGS eddy diffusivity for scalar, and  $C$  and  $l$  are the Smagorinsky constant and length scale.

Sullivan et al. (2007) further improved this model to include the effect of Stokes production and wave breaking by adding three new terms to the right side of (A.1):

$$-u_j^{st} \frac{\partial e}{\partial x_j} - \tau'_{ij} \frac{\partial u_i^{st}}{\partial x_j} + \sum_m W^m$$

where the superscript  $st$  represents Stokes drift, and the effects of  $m = 1, \dots, M$  discrete wave-breaking events are represented by a subgrid-scale TKE generation rate  $W^m$ . Since wave breaking is not considered in this study,  $W^m$  is set to zero for all experiments.

#### References

- Craik, A.D.D., Leibovich, S., 1976. A rational model for Langmuir circulations. *J. Fluid Mech.* 73, 401–426. <http://dx.doi.org/10.1017/S0022112076001420>.
- D'Asaro, E.A., 2001. Turbulent vertical kinetic energy in the ocean mixed layer. *J. Phys. Oceanogr.* 31 (12), 3530–3537.
- D'Asaro, E.A., 2014. Turbulence in the upper-ocean mixed layer. *Annu. Rev. Mar. Sci.* 6, 101–115.
- Dean, R.G., Dalrymple, R.A., 1991. *Water Wave Mechanics for Engineers and Scientists*. World Sci., Singapore, p. 353.
- Fairall, C.W., Bradley, E.F., Hare, J.E., Grachev, A.A., Edson, J.B., 2003. Bulk parameterization of air sea fluxes: updates and verification for the COARE algorithm. *J. Clim.* 16, 571–590.
- Fan, Y., Griffies, S.M., 2014. Impacts of parameterized Langmuir Turbulence and nonbreaking wave mixing in global climate simulations. *J. Clim.* 27, 4752–4775.
- Fan, Y., Jarosz, E., Yu, Z., Rogers, E.W., Jensen, T.G., Liang, J.-H., 2018. Langmuir turbulence in horizontal salinity gradient. *Ocean Modell.* 129, 93–103. <http://dx.doi.org/10.1016/j.ocemod.2018.07.010>.
- Fan, Y., Lin, S.-J., Griffies, S.M., Hemer, M.A., 2014. Simulated global swell and wind-sea climate and their responses to anthropogenic climate change at the end of the twenty-first century. *J. Clim.* 27, 3516–3536.

- Gargett, A.E., Wells, J.R., 2007. Langmuir turbulence in shallow water. Part 1. Observations. *J. Fluid Mech.* 576, 27–61. <http://dx.doi.org/10.1017/S0022112006004575>.
- Gargett, A.E., Wells, A.E., Grosch, C.E., 2004. Langmuir supercells: A mechanism for sediment resuspension and transport in shallow seas. *Science* 306, 1925–1928.
- Grant, A.L.M., Belcher, S.E., 2009. Characteristics of Langmuir turbulence in the ocean mixed layer. *J. Phys. Oceanogr.* 39, 1871–1887. <http://dx.doi.org/10.1175/2009JPO4119.1>.
- Hamlington, P.E., Van Roekel, L.P., Fox-kemper, B., Julien, K., Chini, G.P., 2014. Langmuir–submesoscale interactions: Descriptive analysis of multiscale frontal spindown simulations. *J. Phys. Oceanogr.* 44, 2249–2272. <http://dx.doi.org/10.1175/JPO-D-13-0139.1>.
- Harcourt, R.R., D'Asaro, E.A., 2008. Large-eddy simulation of langmuir turbulence in pure wind seas. *J. Phys. Oceanogr.* 38, 1542–1562. <http://dx.doi.org/10.1175/2007JPO3842.1>.
- Kukulka, T., Harcourt, R.R., 2017. Influence of Stokes drift decay scale on Langmuir turbulence. *J. Phys. Oceanogr.* 1637–1656.
- Kukulka, T., Plueddemann, A.J., Trowbridge, J.H., Sullivan, P.P., 2009. Significance of Langmuir circulation in upper ocean mixing: Comparison of observations and simulations. *Geophys. Res. Lett.* 36, L10603. <http://dx.doi.org/10.1029/2009GL037620>.
- Kukulka, T., Plueddemann, A.J., Trowbridge, J.H., Sullivan, P.P., 2010. Rapid mixed layer deepening by the combination of Langmuir and shear instabilities: A case study. *J. Phys. Oceanogr.* 40, 2381–2400. <http://dx.doi.org/10.1175/2010JPO4403.1>.
- Kukulka, T., Plueddemann, A.J., Trowbridge, J.H., Sullivan, P.P., 2011. The influence of crosswind tidal currents on Langmuir circulation in a shallow ocean. *J. Geophys. Res.* 116, C08005. <http://dx.doi.org/10.1029/2011JC006971>.
- Large, W.G., McWilliams, J.C., Doney, S.C., 1994. Oceanic vertical mixing: a review and a model with a nonlocal boundary layer parameterization. *Rev. Geophys.* 32, 363–403.
- Li, Q., Fox-Kemper, B., 2017. Assessing the effects of langmuir turbulence on the entrainment buoyancy flux in the ocean surface boundary layer. *J. Phys. Oceanogr.* 47, 2863–2886. <http://dx.doi.org/10.1175/JPO-D-17-0085.1>.
- Li, M., Garrett, C., Skillingstad, E., 2005. A regime diagram for classifying turbulent large eddies in the upper ocean. *Deep-Sea Res.* 1 52 (2), 259–278.
- Li, Q., Webb, A., Fox-Kemper, B., Craig, A., Danabasoglu, G., Large, W.G., Vertenstein, M., 2016. Langmuir mixing effects on global climate: WAVEWATCH III in CESM. *Ocean Model.* 103, 145–160. <http://dx.doi.org/10.1016/j.ocemod.2015.07.020>.
- Li, M., Zahariev, K., Garrett, C., 1995. Role of Langmuir circulation in the deepening of the ocean surface mixed layer. *Science* 270, 1955–1957.
- Liang, J.-H., Deutsch, C., McWilliams, J.C., Baschek, B., Sullivan, P.P., Chiba, D., 2013. Parameterizing bubble-mediated air-sea gas exchange and its effect on ocean ventilation. *Glob. Biogeochem. Cycles* 27, 894–905. <http://dx.doi.org/10.1002/gbc.20080>.
- Liang, J.-H., Emerson, S.R., D'Asaro, E.A., McNeil, C.L., Harcourt, R.R., Sullivan, P.P., Yang, B., Cronin, M.F., 2017. On the role of sea-state in bubble-mediated air-sea gas flux during a winter storm. *J. Geophys. Res.* 122, 2671–2685.
- Louis, J.F., 1979. A parametric model of vertical eddy fluxes in the atmosphere. *Bound.-Layer Meteorol.* 17, 187–202.
- Lygre, A., Krogstad, H.E., 1986. Maximum entropy estimation of the directional distribution in ocean wave spectra. *J. Phys. Oceanogr.* 16, 2052–2060.
- McWilliams, J.C., Huckle, E., Liang, J.-H., 2012. The wavy Ekman layer: Langmuir circulations, breaking waves, and Reynolds stress. *J. Phys. Oceanogr.* 42, 1793–1816.
- McWilliams, J.C., Huckle, E., Liang, J.-H., Sullivan, P.P., 2014. Langmuir turbulence in swell. *J. Phys. Oceanogr.* 44, 870–890. <http://dx.doi.org/10.1175/JPO-D-13-0122.1>.
- McWilliams, J.C., Sullivan, P.P., 2000. Vertical mixing by Langmuir circulations. *Spill Sci. Technol. Bull.* 6 (3/4), 225–237.
- McWilliams, J.C., Sullivan, P.P., Hoeng, C., 1997. Langmuir turbulence in the Ocean. *J. Fluid Mech.* 334, 1–30.
- Min, H.S., Noh, Y., 2004. Influence of the surface heating on Langmuir circulation. *J. Phys. Oceanogr.* 34, 2630–2641. <http://dx.doi.org/10.1175/JPOJPO-2654.1>.
- Moeng, C.-H., 1984. A large-eddy simulation model for the study of planetary boundary-layer turbulence. *J. Atmos. Sci.* 41, 2052–2062.
- Pearson, B., 2018. Turbulence-induced anti-stokes flow and the resulting limitations of large-eddy simulation. *J. Phys. Oceanogr.* 48, 117–122. <http://dx.doi.org/10.1175/JPO-D-17-0208.1>.
- Qiao, F., Yuan, Y., Yang, Y., Zheng, Q., Xia, C., Ma, J., 2004. Wave-induced mixing in the upper ocean: Distribution and application to a global ocean circulation model. *Geophys. Res. Lett.* 31, L11303. <http://dx.doi.org/10.1029/2004GL019824>.
- Rabe, T.J., Kukulka, T., Ginis, I., Hara, T., Reichel, B.G., 2015. Langmuir turbulence under hurricane Gustav (2008). *J. Phys. Oceanogr.* 45, 657–677.
- Reichl, B.G., Wang, D., Hara, T., Ginis, I., Kukulka, T., 2016. Langmuir turbulence parameterization in tropical cyclone conditions. *J. Phys. Oceanogr.* 46, 863–886. <http://dx.doi.org/10.1175/JPO-D-15-0106.1>.
- Skyllingstad, E.D., Denbo, D.W., 1995. An ocean large-eddy simulation of Langmuir circulations and convection in the surface mixed layer. *J. Geophys. Res.* 100 (5), 8501–8522.
- Smyth, W.D., Skillingstad, E.D., Crawford, G.B., Wijesekera, H., 2002. Nonlocal fluxes and Stokes drift effects in the K-profile parameterization. *Ocean Dyn.* 52, 104–115.
- Sullivan, P.P., McWilliams, J.C., Melville, W.K., 2007. Surface gravity wave effects in the oceanic boundary layer: large-eddy simulation with vortex force and stochastic breakers. *J. Fluid Mech.* 593, 405–452. <http://dx.doi.org/10.1017/S002211200700897X>.
- Sullivan, P.P., Romero, L., McWilliams, J.C., Melville, W.E., 2012. Transient evolution of Langmuir turbulence in ocean boundary layers driven by hurricane winds and waves. *J. Phys. Oceanogr.* 42, 1959–1980.
- Tejada-Martínez, A.E., Grosch, C.E., 2007. Langmuir turbulence in shallow water. Part 2. Large-eddy simulation. *J. Fluid Mech.* 576, 63–108.
- Ulate, M., Wang, Q., Haack, T., Holt, T., Alappattu, D.P., 2019. Mean offshore refractive conditions during the CASPER east field campaign. *J. Appl. Meteor. Climatol.* 58, 853–874. <http://dx.doi.org/10.1175/JAMC-D-18-0029.1>.
- Van Roekel, L.P., Fox-Kemper, B., Sullivan, P.P., Hamlington, P.E., Haney, S.R., 2012. The form and orientation of Langmuir cells for misaligned winds and waves. *J. Geophys. Res.* 117, 1–22.
- Walker, R., Tejada-Martínez, A.E., Grosch, C.E., 2016. Large-Eddy simulation of a coastal ocean under combined effects of surface heat flux and full-depth Langmuir circulation. *J. Phys. Oceanogr.* 46, 2411–2436. <http://dx.doi.org/10.1175/JPO-D-15-0168.1>.
- Wang, D., Kukulka, T., Reichl, B.G., Hara, T., Ginis, I., 2018b. Interaction of Langmuir turbulence and inertial currents in the ocean boundary layer under tropical cyclones.
- Wang, D., Kukulka, T., Reichl, B.G., Hara, T., Ginis, I., 2019. Wind-wave misalignment effects on Langmuir turbulence in tropical cyclone conditions. *J. Phys. Oceanogr.* 49, 3109–3126. <http://dx.doi.org/10.1175/JPO-D-19-0093.1>.
- Wang, S., Wang, Q., Doyle, J., 2002. Some improvements to Louis surface flux parameterization. In: 15th Symp. on Boundary Layers and Turbulence. Amer. Meteor. Soc., Wageningen, Netherlands, pp. 547–550, Preprints.
- Wang, Q., et al., 2018a. CASPER: Coupled air-sea processes and electromagnetic (EM) ducting research. *Bull. Amer. Meteorol. Soc.* <http://dx.doi.org/10.1175/BAMS-D-16-0046.1>.